Structure and thermal evolution of exoplanetary cores

Irene Bonati[1], Marine Lasbleis[2], and Lena Noack[3]

[1]Tokyo Institute of Technology
[2]Laboratoire de planetologie et geodynamique, LPG, CNRS
[3]Freie Universität Berlin

November 26, 2022

Abstract

Most of the large terrestrial bodies in the solar system display evidence of past and/or current magnetic activity, which is thought to be driven by thermo-chemical convection in an electrically conducting fluid layer. The discovery of a large number of extrasolar planets motivates the search of magnetic fields beyond the solar system. While current observations are limited to their radius and minimum mass, studying the evolution of exoplanetary magnetic fields and their interaction with the atmosphere can open new avenues for constraining interior properties from future atmospheric observations.

Here, we investigate the evolution of massive planets ($0.8-2$~$M_{\rm Earth}$) with different bulk and mantle iron contents. Starting from their temperature profiles at the end of accretion, we determine the structure of the core and model its subsequent thermal and magnetic evolution over 5~Gyr. We find that the planetary iron content strongly affects core structure and evolution, as well as the lifetime of a magnetic field. Iron-rich planets feature large solid inner cores which can grow up to the liquid outer core radius, shutting down any pre-existing magnetic activity. As a consequence, the longest magnetic field lifetimes (~ 4.15~Gyr) are obtained for planets with intermediate iron inventories ($50-60$~wt.\%). The presence of a small fraction of light impurities keeps the core liquid for longer and extends the magnetic field lifetime to more than 5~Gyr. Even though the generated magnetic fields are too weak to be detected by ground facilities, indirect observations can help shedding light on exoplanetary magnetic activity.

Structure and thermal evolution of exoplanetary cores

Irene Bonati[1], Marine Lasbleis[1,2], and Lena Noack[3]

[1]Earth-Life Science Institute, Tokyo Institute of Technology, Tokyo 152-8550, Japan
[2]Laboratoire de Planétologie et Géodynamique, LPG, UMR 6112, CNRS, Université de Nantes, Université d'Angers, France
[3]Department for Earth Sciences, Freie Universität Berlin, Malteserstr. 74-100, D-12249 Berlin, Germany

Key Points:

- We investigate the evolution of the cores of rocky planets with masses between 0.8 and 2 Earth masses and variable bulk and mantle iron contents.
- The content and distribution of iron in a planetary body influences core evolution and magnetic field lifetimes significantly.
- Despite producing stronger magnetic fields, the cores of iron-rich planets tend to become mostly or completely solid, which shortens the dynamo lifetime.

Corresponding author: Irene Bonati, `irene.bonati@elsi.jp`

Abstract

Most of the large terrestrial bodies in the solar system display evidence of past and/or current magnetic activity, which is thought to be driven by thermo-chemical convection in an electrically conducting fluid layer. The discovery of a large number of extrasolar planets motivates the search of magnetic fields beyond the solar system. While current observations are limited to their radius and minimum mass, studying the evolution of exoplanetary magnetic fields and their interaction with the atmosphere can open new avenues for constraining interior properties from future atmospheric observations. Here, we investigate the evolution of massive planets ($0.8-2\ M_{\mathrm{Earth}}$) with different bulk and mantle iron contents. Starting from their temperature profiles at the end of accretion, we determine the structure of the core and model its subsequent thermal and magnetic evolution over 5 Gyr. We find that the planetary iron content strongly affects core structure and evolution, as well as the lifetime of a magnetic field. Iron-rich planets feature large solid inner cores which can grow up to the liquid outer core radius, shutting down any pre-existing magnetic activity. As a consequence, the longest magnetic field lifetimes (~ 4.15 Gyr) are obtained for planets with intermediate iron inventories ($50-60$ wt.%). The presence of a small fraction of light impurities keeps the core liquid for longer and extends the magnetic field lifetime to more than 5 Gyr. Even though the generated magnetic fields are too weak to be detected by ground facilities, indirect observations can help shedding light on exoplanetary magnetic activity.

Plain Language Summary

Earth's magnetic field is powered by vigorous convection in its liquid metallic outer core. The presence of a magnetic field is thought to help the stability of habitable surface conditions by shielding the planetary upper atmosphere from harmful solar radiation. Most rocky planets in our solar system display past or present signatures of magnetic activity, and a similar trend might exist in exoplanetary systems. So far, our knowledge on exoplanets relies on their radii and masses, while interior properties remain largely unconstrained. Studying the evolution of exoplanetary magnetic fields and their interaction with the surrounding environment will help constraining interior properties from future atmospheric observations. Here, we investigate the structure and the thermal and magnetic evolution of the cores of rocky planets with different masses (0.8-2 Earth masses) and variable bulk and mantle iron contents. We find that the iron content and its internal distribution between a planet's core and mantle strongly affects the evolution of the core and the lifetime of a magnetic field. Despite producing stronger magnetic fields, iron-rich planets tend to grow fully solid cores, thus hindering any further magnetic activity. The presence of a small fraction of light core impurities can help prolong magnetic field lifetimes.

1 Introduction

Most of the large rocky bodies in the solar system present evidence of past and/or present magnetic activity (Stevenson et al., 1983; Breuer et al., 2010; Schubert & Soderlund, 2011), with the potential exception of Venus, for which no current magnetic field has been detected and no record of past activity is available (Konopliv & Yoder, 1996; Nimmo, 2002; Zhang et al., 2016; Dumoulin et al., 2017). Magnetic fields are generated through the dynamo effect in a large volume of an electrically conducting liquid in the planet's interior. Earth's magnetic field has been operating for about 3.45 Gyr (Tarduno et al., 2010) and is thought to be mainly sustained by the crystallisation of its central solid inner core, powering thermo-chemical convection in the liquid outer core by the release of light-element enriched material and latent heat (Braginsky, 1963). The geodynamo is thus the result of the secular cooling of Earth's interior (Labrosse, 2003; Buffett, 2003). In principle, the existence of a magnetic field is considered as evidence for a planet's internal dynamics, as well as for the existence of an electrically conducting layer at depth. While being topic of active debate (T. E. Moore & Horwitz, 2007; Strangeway et al., 2010; Brain et al., 2013), planetary magnetism may also play an important role for the development of habitable surface conditions and their long-term stability of planetary bodies, as it shields the upper atmosphere from mass loss induced by stellar winds and extreme space weather events (Dehant et al., 2007; Lammer et al., 2018; Del Genio et al., 2020).

The importance of magnetism for planetary evolution and/or habitability strongly motivates the search and the study of magnetic fields beyond the solar system. To date, more than 4000 planetary candidates have been detected (Schneider et al., 2011; Akeson et al., 2013), with many of the bodies lying in the super-Earth regime, comprising planets with masses larger than Earth but smaller than Neptune. Despite the large number of discovered exoplanets, knowledge regarding their internal structure is lacking (Spiegel et al., 2014; Baraffe et al., 2014), as current observations are limited to providing the planetary radius and/or its (minimum) bulk mass. While inferences on a planet's interior can be drawn to some degree, the internal structures and dynamic patterns matching these two constraints are manifold (Rogers & Seager, 2010; Howe et al., 2014). This degeneracy constitutes a major barrier for obtaining unique solutions for planets' interior structures.

The ability of a planet to sustain habitable surface conditions is, however, strongly linked to its interior structure and dynamics (Noack et al., 2014). The detection and measurement of exoplanetary magnetic fields would help shedding light on the internal structure and dynamics of extra-solar bodies, on the frequency of planetary magnetic fields in the Universe, as well as on the importance of magnetic activity for the emergence of planetary habitability. However, no direct observation of magnetic fields beyond our solar system exists to this date. Such observations remain challenging due to the limited sensitivity of current instrumentation, which is too low to detect the weak magnetic fields exerted by small rocky planets (Driscoll & Olson, 2011). Upcoming missions aimed at the investigation of exoplanetary atmospheres (e.g., JWST, ARIEL, WFIRST) will enable additional characterization of exoplanetary bodies (Gardner et al., 2006; Spergel et al., 2015). Until then, theoretical modelling can provide a means for understanding and constraining interactions and feedback mechanisms between a planet's interior and its atmosphere. Magnetic fields are well suited for this purpose, as they span a planet in its entirety, being generated in the deepest portion of the interior and manifesting in the upper layers of the atmosphere.

Past modelling efforts investigating exoplanetary interiors have led to the development of simple scaling laws for deriving the internal structure (core and planetary radii) and dynamic properties (likelihood of plate-tectonics-like behaviour) of super-Earths (Valencia et al., 2006; Seager et al., 2007). These relations often assume a core-mantle boundary (CMB) heat flux proportional to the planetary mass, as well as an Earth-like composition. Scaling laws providing estimates for the magnetic field intensity at the CMB based on the available energy for dynamo generation have been devised as well (Olson & Christensen, 2006; Aubert et al., 2009), and have been extensively used by both the geophysical and the planetary science communities (Driscoll & Olson, 2011; López-Morales et al., 2011; McIntyre et al., 2019). Driscoll and Olson (2011) have considered optimal conditions for dynamo generation in $1-10\ M_{\mathrm{Earth}}$ planets. Such optimal dynamos are driven by vigorous convection in the core due to fast cooling across the CMB and vigorous convection in the mantle. Very recently, Boujibar et al. (2020) have determined internal structures at the end of accretion for super-Earths with core mass fractions corresponding to Earth, Mars and Mercury.

The interior structures (e.g., core mass fraction, convective radius in the liquid outer core) of the planets in the studies mentioned above are based on bodies in our solar system (Earth, Mercury, and Mars). However, depending on their mass and composition, planetary bodies can cover a large variety of possible structures and sizes. This diversity is a result of different disk composition (Bond et al., 2010; Moriarty et al., 2014), accretion processes, and the differentiation history. In addition, the distribution of iron between core and mantle, which is strongly tied to accretion and differentiation processes (Elkins-Tanton & Seager, 2008; Wohlers & Wood, 2017), has also strong implications for the final planetary structure, as well as for melting temperatures, viscosity, thermodynamic and transport properties such as electric conductivity, and the resulting dynamics of the mantle and/or core. As a result, different structures and compositions can have important influences on the generated magnetic fields (Driscoll & Olson, 2011), and it is thus important to conduct a parameter exploration.

Here, we investigate the core evolution of bodies with variable masses and iron contents (bulk and mantle), assuming Earth-like mineral assemblages. Starting from their internal structure after the solidification of molten silicates at the CMB (Stixrude, 2014; Noack & Lasbleis, 2020), we determine the initial core structure and model its subsequent thermal and magnetic evolution by computing inner core growth, buoyancy fluxes, and the strength and lifetime of the generated magnetic field. The manuscript is structured as follows: In Section 2 we briefly introduce the interior structure and the mantle evolution model (Section 2.1), as well as thermal evolution model for the core (Section 2.2). We then present the core evolution histories obtained by varying the planetary mass, the bulk and mantle iron contents, and the the amount of light alloying components in the core in Section 3.2. We further show the calculated magnetic field strengths and lifetimes in Section 3.3. In Section 4 we discuss our results and parameter uncertainties. A summary can be found in Section 5 together with some concluding remarks.

2 Methods

2.1 Interior structure and mantle evolution model

We obtain internal structures from the code CHIC (Code for Habitability, Interior and Crust; Noack et al. (2017)) for planets with different masses and variable iron contents, leading to different core mass fractions. The explored planetary mass range lies between 0.8 and 2 M_{Earth} (with $M_{\text{Earth}} = 5.972{\cdot}10^{24}$ kg being Earth's mass). We employ bulk weight fractions of iron X_{Fe} between 0.15 and 0.8 (15−80 wt.% Fe: as a reference, Earth has an iron content of about 32 wt.%), and mantle iron numbers $\#Fe_{\text{M}}$ varying between 0 and 0.2 (as a reference, Earth has a mantle iron number $\#Fe_{\text{M}}$ of 0.1). The mantle iron number is defined as the ratio between iron-bearing (FeO, $FeSiO_3$ and Fe_2, SiO_4) and magnesium-rich minerals (MgO, $MgSiO_3$ and Mg_2 SiO_4). The range explored in this study ($\#Fe_{\text{M}} = 0{-}0.2$) corresponds to mantle iron mass fractions $X_{\text{Fe,m}} = 0{-}0.1457$ (see also Noack and Lasbleis (2020)). The interior structure model solves the hydrostatic, Poisson, and mass equations from the planetary centre up to its surface in order to obtain interior pressure, gravity, and mass profiles. The planetary surface pressure is set to 1 bar. Using the planetary mass and the iron contents X_{Fe} and $\#Fe_{\text{M}}$ as inputs, the model determines the planetary structure (core and planetary radius), and the thermodynamic parameter profiles self-consistently.

The model assumes an Earth-like mantle mineralogy (Mg, Fe, Si, and O) and phase transitions, with a mantle consisting of ($\text{Mg}_{1-\#Fe_{\text{M}}}$, $\text{Fe}_{\#Fe_{\text{M}}}$)O and SiO_2. Even though some exoplanets might be rich in other elements (e.g., aluminium, calcium, carbon) and display completely different chemistries (Kuchner & Seager, 2005; Dorn et al., 2019), it is likely for planetary building blocks located inside the snow line to have mineralogies similar to planets in the inner solar system, with slight variations in the Mg, Fe, and Si contents depending on the host star's metallicity (Bitsch & Battistini, 2020). A third-order Birch-Murnaghan (Stixrude et al., 2009) and a Holzapfel (Bouchet et al., 2013) equations of state are used for the mantle and the core (pure iron), respectively. Interior structures of planets with masses beyond 2 M_{Earth} are not explored, as the employed equations of state are devised for Earth's pressure range, and an extrapolation to higher pressures would lead to errors due to missing data from experiments and ab initio simulations. We therefore set the upper planetary mass limit to 2 M_{Earth}, for which we have robust equations of state for both mantle and core that we can employ (Hakim et al., 2018). For more details about the interior structure model, the reader is redirected to the papers by Noack et al. (2017), and to Noack and Lasbleis (2020) for parameterizations of interior properties of massive rocky planets.

2.1.1 Thermal profiles of the core

Recent studies have stressed the importance of both the initial structure and the thermal profile of a planet, as they set the stage for its subsequent evolution and tectonic behaviour (Stein et al., 2004; Breuer et al., 2010; Stamenković et al., 2012; Stamenković & Breuer, 2014; ONeill et al., 2016; Dorn et al., 2018). Estimating the energy budget of bodies during and in the aftermath of accretion is challenging, even for planets in the solar system due to the many unconstrained thermodynamic and transport parameters. Here, we use initial temperature profiles corresponding to the 'hot' scenarios in Noack and Lasbleis (2020). These are high temperature end-members of the profiles in Stixrude (2014), determined for planets with an Earth-like composition and variable mass. These profiles describe planets at the late stage of planet formation, right after the full crystallisation of the silicates at the CMB. This solidified material is a portion of a (global) magma ocean, which is likely to be present in the aftermath of accretion (Abe, 1997; Canup, 2004; Nakajima & Stevenson, 2015). Typically, solidification of such a magma ocean proceeds from the bottom of the mantle towards the surface (Andrault et al., 2011; Monteux et al., 2016), but middle-out crystallisation processes potentially leading to the preservation of a basal magma ocean for billions of years have been proposed as well (Labrosse et al., 2007; Stixrude et al., 2009; Nomura et al., 2011).

2.1.2 Melting curves and inner core size

We use formulations for melting curves for iron and rock components in super-Earths interiors, which were proposed in Stixrude (2014) based on existing experimental results, ab initio data, and scaling laws. The melting temperature of the mantle for pressures $P > 17$ GPa is defined as

$$T_{\mathrm{m,mantle}} = 5400 \left(\frac{P}{140 \cdot 10^9} \right)^{0.48} \frac{1}{1 - \ln(1 - \#Fe_{\mathrm{M}} - X_{\mathrm{M}})}. \tag{1}$$

with pressure P in Pascal and temperature T in Kelvin. X_{M} is the difference between liquidus and solidus temperatures. As stated previously, the mantle iron number $\#Fe_{\mathrm{M}}$ defines the ratio between iron and magnesium-bearing minerals present in the mantle, which are assumed to be similar to Earth. An increase of $\#Fe_{\mathrm{M}}$ exerts an effect similar to the light elements in the core and leads to a reduction of the mantle melting temperature $T_{\mathrm{m,mantle}}$ (Dorn et al., 2018). Similarly, the mantle melting temperature decreases with variations in the mantle composition, which is reflected with the parameter X_{M}. Earth's current mantle melting temperature is best matched with $\#Fe_{\mathrm{M}}$=0.1 and X_{M}=0.11 (Stixrude, 2014), and which we refer to as warm profile (mimicking the solidus melting temperature of the mantle). The case with X_{M}=0 is referred to as hot profile (mimicking the liquidus melting temperature of the mantle).

The melting temperature for pure iron in Stixrude (2014) is based on Morard et al. (2011), and is defined as

$$T_{\mathrm{m,core}} = 6500 \left(\frac{P}{340 \cdot 10^9} \right)^{0.515} \frac{1}{1 - \ln(1 - x)}, \tag{2}$$

where P is the pressure (in Pa) and x is the mole fraction of light components in the core. The x dependence in Equation (2) reflects the reduction of the core melting tempera-

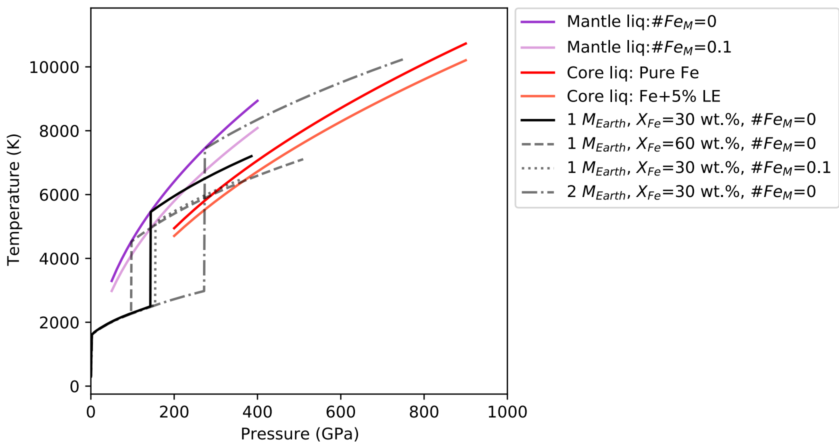

Figure 1. Initial temperature profiles for planets with masses of 1 and 2 M_{Earth}, bulk iron contents X_{Fe} of 30 wt.% and 60 wt.%, and mantle iron numbers $\#Fe_{\mathrm{M}}$ of 0 and 0.1. The purple and red solid curves display mantle liquidus curves for different mantle iron numbers ($\#Fe_{\mathrm{M}}$ of 0 and 0.1) and core liquidus curves for different core compositions (a pure iron core and a core containing iron and 5% of light elements), respectively. All profiles are consistent with the 'hot' scenario (Noack & Lasbleis, 2020), following which the temperature at the CMB is anchored to the mantle liquidus at that pressure.

ture due to the presence of light elements. Earth's outer core is thought to contain about 5−10% of light elements, which were imparted during accretion and core formation (Wood et al., 2006; Rubie et al., 2011; Badro et al., 2015). The presence of light elements in Earth's core compensates for the temperature jump at the inner core boundary (ICB), which does not correspond to a pure phase change (Hirose et al., 2013; Badro et al., 2015). Although the identity of these components remains elusive, seismology and mineral physics studies have proposed oxygen, silicon, sulfur, carbon, and hydrogen as potential candidates (Hirose et al., 2013). Light elements could be present in the cores of massive exoplanets with masses up to 2 M_{Earth} as well, although likely candidates and their partitioning properties at such high pressures are so far unknown, and need further investigation. For this study, we vary the core light element content between 0 and 10%, and assume that light components are preferentially partitioned into the liquid outer core during evolution.

The employed melting temperatures for the mantle and the core are shown together with the thermal profiles (see Section 2.1.1) in Figure 1, for planets of 1 and 2 M_{Earth} with variable bulk iron contents X_{Fe} (30 wt.% and 60 wt.%) and mantle iron numbers $\#Fe_{\mathrm{M}}$ (0 and 0.1). The mantle and core melting temperatures are reduced with the addition of iron and light impurities, respectively. The thermal profiles are high temperature end-member scenarios of the ones in Stixrude (2014) and imply a hot core, where the uppermost core temperature is anchored to the mantle liquidus that varies according to the mantle iron content. The temperature jump at the CMB is calculated for every planet depending on its internal structure and thermodynamic parameters (see Noack and Lasbleis (2020) for further details).

2.1.3 Polynomial fitting of interior profiles

Noack and Lasbleis (2020) provided a suite of parameterizations for average thermodynamic parameters in both the mantle and the core. In order to model the evolution of the metallic core, we need its pressure-dependent density profile. Following the work of Labrosse (2015) of fitting the Preliminary Reference Earth Model (PREM) for the Earth, we fit the initial interior profiles obtained using the model described in Section 2.1. The core density is fitted using a polynomial function with three parameters: the density at the planetary centre ρ_0, the typical length scale for density variations L_ρ, and a second-order variation A_ρ as

$$\rho(r) = \rho_0 \left(1 - \frac{r^2}{L_\rho^2} - A_\rho \frac{r^4}{L_\rho^4}\right) \tag{3}$$

with

$$L_\rho = \sqrt{\frac{3K_0}{2\pi G \rho_0^2}}; \quad A_\rho = \frac{5K_0' - 13}{10}, \tag{4}$$

where $K = K_0 + K_0'(P - P_0)$ is the bulk modulus, which is considered pressure-dependent and is anchored at the planetary centre (labelled by the subscript 0), and G is the gravitational constant ($G = 6.67430 \cdot 10^{-11}$ m^3 kg^{-1} s^{-2}). P_0 and K_0' are the pressure and the pressure derivative of the bulk modulus at the planetary centre, respectively.

Integrating the gravity using Gauss' theorem and assuming the system is in hydrostatic equilibrium, the gravity and pressure profiles $g(r)$ and $P(r)$ are

$$g(r) = \frac{4\pi}{3} G \rho_0 r \left(1 - \frac{3}{5}\frac{r^2}{L_\rho^2} - \frac{3A_\rho}{7}\frac{r^4}{L_\rho^4}\right), \tag{5}$$

$$P(r) = P_0 - K_0 \left(\frac{r^2}{L_\rho^2} - \frac{4}{5}\frac{r^4}{L_\rho^4}\right). \tag{6}$$

K_0 is calculated as

$$K_0 = \frac{2}{3}\pi L_\rho^2 \rho_0^2 G. \tag{7}$$

We assume that the core density does not evolve with time, although light elements are expelled into the liquid phase as a solid inner core grows. As a result, we neglect both the thermal and chemical dependence of the density compared to the one related to pressure variations. The temperature profile $T(r)$ is assumed to be isentropic, that is, with γ being the Grüneisen parameter,

$$\left(\frac{\partial T}{\partial \rho}\right)_{\mathrm{S}} = \gamma. \tag{8}$$

Anchoring this temperature profile to the radius r_0 with density $\rho(r_0)$, and assuming a constant γ (obtained by averaging the Grüneisen parameter over the volume of the fully liquid outer core), the temperature profile is given by

$$T(r) = T(r_0) \left(\frac{\rho(r)}{\rho(r_0)}\right)^\gamma. \tag{9}$$

The radius r_0 is chosen as either the planetary centre (i.e., $r_0 = 0$) when there is (still) no inner core, or the inner core radius r_{IC} once the inner core starts forming (see Section 2.2 for more details).

2.1.4 Mantle thermal evolution model

Starting from the temperature profiles as depicted in Figure 1, based on Noack and Lasbleis (2020), we simulate the long-term thermal evolution of the mantle over 5 Gyr.

Based on the heat loss from mantle to surface by both convection and conductive heat flow, we can estimate how strong the core cools over time, and finally, how the heat flux at the CMB varies over time. Estimating the evolution of the heat flow at a planet's CMB is challenging. For the Earth, estimates of the present CMB heat flow range between $\sim 5-17$ TW (Lay et al., 2008), and its lateral variation and evolution remain unclear. As a result, past work has assumed either a constant CMB heat flow over the entirety of a planet's evolution (Labrosse, 2003), or a CMB heat flow following an exponentially decaying curve (Labrosse, 2015). However, time-dependent reversal frequency excludes both, meaning that an oscillatory CMB heat flux is needed.

Here, we employ the mantle convection code CHIC (Noack et al., 2017) to obtain the CMB heat flow for planets of different mass and iron contents (bulk and mantle). The model solves the conservation equations for mass, momentum, and energy in a 2-D quarter sphere using the spherical annulus geometry (Hernlund & Tackley, 2008), which is able to reproduce thermal evolution scenarios similarly to a 3-D sphere while using much less computational power. We model compressional convection under the truncated anelastic liquid approximation (TALA), where thermodynamic reference profiles for parameters such as density, thermal expansion coefficient and heat capacity are calculated as described in Noack and Lasbleis (2020). During the evolution, radiogenic elements heat up the mantle, which decay over time and are assumed to start with Earth-like concentrations (McDonough & Sun, 1995).

The mantle is also heated from below due to core cooling. The heat flux of the core mantle boundary is here determined only from the mantle side, assuming that the thick thermal boundary forming at the bottom of the mantle dominates how much heat is taken up into the mantle, and therefore controls the heat loss from the core. In the mantle evolution simulations, the core is otherwise not considered, i.e. no energy contribution from freezing of the core (latent heat or gravitational energy release) is considered. The obtained CMB heat flow is then used to *a posteriori* compute the energy inputs resulting from secular cooling, latent heat, and gravitational heat release (Equation (10)) at different stages of evolution, but is not taken into account for the mantle evolution simulations. We do consider, however, melt formation in the upper mantle, which has a direct impact on the thermal evolution of the mantle due to latent heat consumption upon melting. We assume that melt is then delivered instantaneously to the surface, leading to a net loss of thermal energy over time. Another factor that impacts the thermal evolution of the mantle is the viscosity of the silicate rocks, which we assume here to be dry but otherwise Earth-like (Noack et al., 2017), using the viscosity laws from Karato and Wu (1993) for the upper mantle and Tackley et al. (2013) for the lower mantle. For the latter, it should be noted that the viscosity in Tackley et al. (2013) was taken to be two orders of magnitude higher than realistic to allow for faster convection simulation, which we did not include here to better mimic the lower mantle rheology for Earth-like materials. In this study we were not particularly interested in local convective features but rather the general, long-term thermal evolution of the mantle. We therefore used a coarse radial resolution of 50 km, with in average similar lateral resolution (but varying with radius due to the spherical shape of the mantle) to save computational costs. In Dorn et al. (2018) we could already show that the mantle resolution (there going down to a radial resolution of 10 km) does not have a strong effect on the thermal evolution of the mantle.

The modelled planets are in a stagnant lid tectonic configuration, featuring a unique rigid plate that does not break up and sink into the mantle in a subduction-like manner. While cooling of the mantle due to melting is taken into account, we do not model that due to eruption of magma to the surface, the colder lithosphere would sink further down into the mantle, hence additionally cooling the mantle (as suggested in the so-called heat-pipe model (W. B. Moore & Webb, 2013). Furthermore, if plate tectonics would be considered, subduction of the cooler lithosphere into the mantle would lead to an additional cooling of the mantle, triggering higher heat fluxes at the CMB than modelled here. However, it is yet unclear how likely plate tectonics is on rocky planets, as Earth is the only rocky body we know of so far that experiences plate tectonics (though speculations exist for our sister planet Venus). Furthermore, Stamenković et al. (2012) could show that at least for super-Earths, the heat flux at the CMB is not affected by the surface mobilisation regime, since a strong cooling of the upper mantle leads to a decoupling of the upper and lower pat of the mantle, leading to similar long-term heat flux patterns at the CMB. For this reason we limit our study here to stagnant-lid planets.

2.2 Core evolution model

2.2.1 Energy balance

Starting from the initial profiles described in Section 2.1, we model the subsequent thermal and magnetic evolution of the core for planets of different mass and iron contents (bulk and mantle). To do this, we design a 1-D parameterized model tracking inner core growth and calculating the core energy budget, the buoyancy fluxes, and the magnetic dipole moment. This is performed using an energy balance approach, which has been extensively used in past studies investigating the geodynamo (Gubbins, 1977; Lister & Buffett, 1995; Braginsky & Roberts, 1995; Nimmo, 2007; Labrosse, 2003). The main concept behind energy balance models is that the heat flow at the CMB, Q_{CMB}, is equal to the sum of the secular cooling of the outer core Q_{C}, the latent heat from freezing of the inner core Q_{L}, the gravitational heat due to the light element release at the ICB Q_{G}, and heat generated from radioactive decay Q_{R} (see Figure 2) as

$$Q_{\mathrm{CMB}} = Q_{\mathrm{C}} + Q_{\mathrm{L}} + Q_{\mathrm{G}} + Q_{\mathrm{R}} \tag{10}$$

We assume that the heat produced by radioactive decay Q_{R} is negligible, as is often done for Earth. The model is run for 5 Gyr of a planet's evolution, which is a reasonable time interval given current distributions of stellar ages (Frank et al., 2014; Safonova et al., 2016).

2.2.2 Before crystallisation of an inner core

In the absence of an (initial) inner core, and neglecting the heat produced by radioactive decay, the energy balance before inner core crystallisation can be simply expressed as $Q_{\mathrm{CMB}} = Q_{\mathrm{C}}$, where the secular cooling Q_{C} is defined as

$$Q_{\mathrm{C}} = -\int_{V_{\mathrm{C}}} \rho C_{\mathrm{P}} \frac{\partial T_{\mathrm{a}}}{\partial t} \mathrm{dV}. \tag{11}$$

Here, V_{C} is the volume of the core, C_{P} is the specific heat capacity of the core, T_{a} is the adiabatic temperature, and t is time. The adiabatic temperature profile is defined as in Equation (9), and is anchored at the planetary centre $r_0 = 0$ with density ρ_0, as

$$T_{\mathrm{a}}(r,t) = T_0(t)\left(1 - \frac{r^2}{L_\rho^2} - A_\rho \frac{r^4}{L_\rho^4}\right)^{\gamma}, \tag{12}$$

where T_0 is the temperature at the centre. Q_{C} then becomes

$$Q_{\mathrm{C}} = -4\pi C_{\mathrm{p}} \frac{\mathrm{dT_0}}{\mathrm{dt}} \int_0^{r_{\mathrm{OC}}} \left(1 - \frac{r^2}{L_\rho^2} - A_\rho \frac{r^4}{L_\rho^4}\right)^{\gamma+1} r^2 \mathrm{dr}. \tag{13}$$

The integral can either be approximated numerically, or by applying the development described in Eq. A2 in Labrosse (2015). We introduce the notation

$$f_\mathrm{C}(r,\delta) = 3\int_0^r (1 - r^2 - A_\rho r^4)^{1+\delta} r^2 \mathrm{dr}, \tag{14}$$

so that the secular cooling term can be written as

$$Q_\mathrm{C} = -\frac{4}{3}\pi C_\mathrm{P}\rho_0 L_\rho^3 f_\mathrm{C}\left(\frac{r_\mathrm{OC}}{L_\rho},\gamma\right)\frac{\mathrm{dT_0}}{\mathrm{dt}}. \tag{15}$$

Q_C can be rewritten as $Q_\mathrm{C} = \mathrm{P_C}\frac{dT_0}{dt}$, where $\mathrm{P_C}$ is a constant which depends on the global parameters of the core and does not vary with time. The temperature at the centre can finally be written as

$$T_0(t) = T_0(t=0) + \frac{1}{P_\mathrm{C}}\int_0^t Q_\mathrm{CMB}(\tau)\mathrm{d}\tau. \tag{16}$$

Here, Q_CMB is the CMB heat flux obtained from the model of Noack et al. (2017). The onset of inner core crystallisation is assumed to happen when the temperature at the planetary centre reaches the liquidus temperature of the outer core alloy, neglecting the possible existence of a supercooling effect (Huguet et al., 2018).

2.2.3 After crystallisation of an inner core

In addition to the secular cooling term, the energy balance after the onset of inner core solidification needs to account for latent and gravitational heat release (Equation (10)). These terms can be written as

$$\mathrm{Q_C} = -\int_{\mathrm{V_{OC}}} \rho C_\mathrm{P}\frac{\partial T_\mathrm{a}}{\partial t}\mathrm{d}V, \tag{17}$$

$$Q_\mathrm{L} = 4\pi r_\mathrm{IC}^2 \rho\left(r_\mathrm{IC}\right) T_\mathrm{m,core}\left(r_\mathrm{IC}\right)\Delta S\frac{\mathrm{d}r_\mathrm{IC}}{\mathrm{d}t}, \tag{18}$$

$$Q_\mathrm{G} = -\int_{\mathrm{V_{OC}}} \rho\mu'\frac{\partial X}{\partial t}\mathrm{d}V. \tag{19}$$

Here, V_OC is the volume of the outer core, $T_\mathrm{m,core}(r_\mathrm{IC})$ and $\rho(r_\mathrm{IC})$ are the melting temperature and the density at the ICB, ΔS is the entropy of freezing (set to 127 $\mathrm{Jkg^{-1}K^{-1}}$; Hirose et al. (2013)), μ' is the difference between the adiabatic and the chemical potentials at the ICB (see Labrosse (2015) for a more detailed derivation), and $\frac{\partial X}{\partial t}$ is the temporal change of light element mass fraction in the outer core. We calculate the melting temperature of the outer core alloy at the inner core radius $r_\mathrm{IC}(t)$ according to Equation (2), in order to obtain the temperature change at the ICB. The temperature at the CMB is assumed to lie on the adiabatic profile, which is consistent with vigorous convection.

Similar to what was previously shown for a planet with no inner core (Section 2.2.2), we can write each of the terms in Equations (17), (18), and (19) as $Q_\mathrm{X} = \mathrm{P_X}\frac{\mathrm{dr_{IC}}}{\mathrm{dt}}$, where X indicates a given heat contribution (secular cooling, latent heat or gravitational heat). We write these terms similarly as in Labrosse (2015), and redirect the reader to the Appendix of that study for further details.

2.3 Change of outer core composition

If the core contains light elements, its composition will evolve as the inner core solidifies, as a result of the gradual release of such impurities. Seismic velocity anomalies in Earth's core hint to the presence of $5-10\%$ light components (Hirose et al., 2013; Badro et al., 2015), candidates of which are oxygen, silicon, sulfur, carbon, and hydrogen (Poirier, 1994). While their abundance and identity is unknown, it is not implausible for such impurities to be present in the cores of massive exoplanets.

Here we use light element bulk contents ranging between $0-10\%$. Depending on whether there is an inner core or not, the inventory of light elements in the outer core will differ, and is larger for bodies featuring larger solid inner cores. With $M_{\mathrm{OC}}(t)$ being the mass of the outer core and X_0 being the bulk fraction of light elements in the outer core in the absence of an inner core, we can obtain the fraction of light elements in the outer core as a function of time $X(t)$ by assuming that no light components enter the solid as

$$X(t) = \frac{X_0 M_{\mathrm{C}}}{M_{\mathrm{OC}}(t)}, \tag{20}$$

and the mass of the outer core is subsequently calculated as

$$M_{\mathrm{OC}}(t) = 4\pi \int_{r_{\mathrm{IC}}(t)}^{r_{\mathrm{OC}}} \rho(x) x^2 \mathrm{d}x = \frac{4}{3}\pi\rho_0 L_\rho^3 \left[f_{\mathrm{C}}\left(\frac{r_{\mathrm{OC}}}{L_\rho}\right) - f_{\mathrm{C}}\left(\frac{r_{\mathrm{IC}}(t)}{L_\rho}\right)\right]. \tag{21}$$

Therefore, if an inner core starts forming, the fraction of light elements in the outer core as a function of time will increase accordingly. As the outer core becomes gradually enriched in light elements, its composition shifts towards eutectic point in the phase diagram. In case of a binary core composition, the melting point depression by light elements corresponding to the attainment of the eutectic point can be as low as 200 K (Fe-Si at 65 GPa and Fe-O at 50 GPa; Kuwayama and Hirose (2004); Seagle et al. (2008)) or 1500 K (Fe-S at 65 GPa; Morard et al. (2008)). Similar to what proposed in Morard et al. (2011), we limit the melting point depression by light impurities to a maximum $\Delta T_{\mathrm{melt,core}} = 1500$ K. This means that as soon as the melting point depression exerted by the presence of light components becomes higher than this threshold, the light element abundance in the outer core is anchored to a pressure-dependent "eutectic" value, for which the temperature reduction is exactly $\Delta T_{\mathrm{melt,core}} = 1500$ K. During the subsequent evolution stages the light element content in the outer core still increases, albeit less strongly, due to the varying ICB pressure. An additional effect that rises upon reaching the eutectic is that the compositions of the inner and outer core are equal, and the density jump at the ICB goes to zero. This effect is taken into account, as it can shut off magnetic activity if thermal buoyancy is not strong enough.

2.4 Buoyancy fluxes

Displacements of liquid in planetary cores result from both variations in their thermal and chemical structure. Thermally-driven dynamos are generated by a strong, superadiabatic, flux of heat at the CMB. Such a mechanism is thought to act predominantly in the early evolution stages of a planet, when the core is very hot and releases a large amount of heat into the mantle (Del Genio et al., 2020). On the other hand, chemically-driven dynamos may start taking place later in time, once/if a solid inner core starts crystallising. In this scenario, density difference between the liquid and solid metal at the ICB, resulting from the expulsion of light elements in the outer core, can supply substantial energy to drive dynamo activity (Braginsky, 1963). Alternatively, snow mechanisms such as the rise of alloy-rich material (Braginsky, 1963) or the settling of solid iron through a stably stratified layer (Hauck et al., 2006; Rückriemen et al., 2018) located in the immediate proximity of the ICB could provide another source of buoyancy for core convection.

Here, we consider both contributions from thermal and chemical anomalies. As a result, the buoyancy flux is expressed as the sum of the thermal and the chemical buoyancy fluxes F_{T} and F_{X}. Following Driscoll and Olson (2011) we calculate these as

$$F_{\mathrm{T}} = \frac{\alpha g}{\rho C_{\mathrm{P}}} q_{\mathrm{c,conv}} \tag{22}$$

$$F_{\mathrm{X}} = \frac{g_{\mathrm{ICB}}\Delta\rho_{ICB}}{\rho}\left(\frac{r_{\mathrm{IC}}}{r_{\mathrm{OC}}}\right)^2 \frac{\mathrm{d}r_{\mathrm{IC}}}{\mathrm{dt}}, \quad (23)$$

where α is the thermal expansion coefficient, $r_I C$ is the inner core radius, and $q_{\mathrm{c,conv}} = q_{\mathrm{CMB}} - q_{\mathrm{c,ad}}$ is the convective heat flux at the CMB, defined as the difference between CMB and adiabatic heat flux. g_{ICB} is the gravity at the ICB and $\mathrm{d}r_{\mathrm{IC}}/\mathrm{dt}$ is the inner core growth rate. $\Delta\rho_{\mathrm{ICB}}$ is the density jump at the ICB and is calculated using the relation $\Delta\rho_{\mathrm{ICB}} = (\Delta\rho_{\mathrm{ICB,Earth}}/X_{\mathrm{Earth}})X_{\mathrm{planet}}$, with $\Delta\rho_{\mathrm{ICB,Earth}} = 600$ kg.m^{-3} the density jump at Earth's ICB and $X_{\mathrm{Earth}} = 11\%$ is an estimate of Earth's light element content according to the melting temperature used in this study for which the main core component (iron) constitutes 89% of the core. Earth's density jump at the ICB has been determined with two types of seismic data, namely short-period body waves ($\Delta\rho_{\mathrm{ICB}} \sim 520-1100$ kg.m^{-3}; Koper and Pyle (2004); Tkalčić et al. (2009)) and long-period normal modes ($\Delta\rho_{\mathrm{ICB}} \sim 820\pm180$ kg.m^{-3}; Masters and Gubbins (2003)). There is strong uncertainty in the estimates, due to differences in the resolution and accuracy of the techniques, sampling techniques, and data processing. Before an inner core starts forming (and/or in the absence of light components), only temperature changes contribute to buoyancy.

The adiabatic heat flux is defined as

$$q_{\mathrm{c,ad}} = k_{\mathrm{c}} T_{\mathrm{CMB}} r_{\mathrm{OC}}/D_{\mathrm{ad}}^2, \quad (24)$$

where k_{c} is the thermal conductivity of the core and T_{CMB} is the temperature at the CMB, which lies on the adiabat. The thermal conductivity determines how fast heat is conducted through the core into the mantle. Estimates for the thermal conductivity of Earth's core span values between ~ 20 (Konôpková et al., 2016) and ~ 160 W.m^{-1}.K^{-1} (Gomi et al., 2013), with dramatic implication for the lifetime of the magnetic field (Labrosse, 2015). As it is very difficult for high-pressure experiments to attain the pressure range governing the cores of such bodies, thermal conductivities of massive exoplanets are currently not known. However, it is expected that the thermal conductivity of a planet increases with increasing pressure. We therefore use a high thermal conductivity $k_{\mathrm{c}} = 150$ W.m^{-1}.K^{-1} lying in the upper range of Earth's values, in order to obtain conservative estimates for the magnetic field lifetime. We acknowledge, however, that thermal conductivities of super-Earths could reach even higher values, which may affect our results. In the Discussion (Section 4.4) we will present how our results vary when employing different thermal conductivities. D_{ad} is an adiabatic length scale (Labrosse et al., 2001) and amounts to $D_{\mathrm{ad}} \sim 6000$ km for Earth (Labrosse, 2003). We calculate D_{ad} for a given planet as $D_{\mathrm{ad}} = \sqrt{3C_{\mathrm{P}}/2\pi\alpha_0\rho_0 G}$.

2.5 Magnetic field

We calculate the magnetic moment m of a given rocky planet by using the scaling law proposed by Olson and Christensen (2006) as

$$m \simeq 4\pi r_{\mathrm{OC}}^3 \beta \left(\rho/\mu_0\right)^{1/2} \left((F_{\mathrm{T}} + F_{\mathrm{X}})(r_{\mathrm{OC}} - r_{\mathrm{IC}})\right)^{1/3}, \quad (25)$$

where β is a saturation constant for fast rotating dynamos ($\beta = 0.2$), $\mu_0 = 4\pi\cdot10^{-7}$ Hm^{-1} is the magnetic permeability. Here, $r_{\mathrm{OC}} - r_{\mathrm{IC}}$ represents the thickness of the convective shell (i.e., the thickness of the liquid outer core). This quantity is obtained from the core evolution model, and becomes smaller as a solid inner core grows. The buoyancy fluxes F_{T} and F_{X} arising from thermal and chemical anomalies, respectively, are calculated from the core evolution model as well, as described in Section 2.4.

Equation (25) assumes that the magnetic field is dipolar, although we do not exclude that different magnetic field morphologies might be present or arise during evolution, especially for bodies featuring large inner cores and thin convective liquid metal shells. Furthermore, this expression is devised for magnetic fields that are powered by convection in a liquid outer core, although it has recently been suggested that super-Earths can have magnetic fields that are generated inside their mantles instead (Soubiran & Militzer, 2018), where iron-bearing minerals can gain metallic properties. In the present study, we will not consider such a process.

For a self-sustaining dynamo action to be viable, the magnetic Reynolds number $R_\mathrm{m} = v(r_\mathrm{OC}-r_\mathrm{IC})/\eta_\mathrm{m}$, where v is the typical flow velocity and η_m is the magnetic diffusivity, needs to be higher than a critical value $R_\mathrm{m,crit} = 40$, as suggested by numerical dynamo simulations (Christensen & Aubert, 2006; Roberts, 2015). The typical velocity of the convective flow v in the outer core is calculated using the scaling relation by Olson and Christensen (2006)

$$v \simeq 1.3((r_\mathrm{OC} - r_\mathrm{IC})/\Omega)^{1/5}(F_\mathrm{T} + F_\mathrm{X})^{2/5}, \tag{26}$$

where Ω is the rotation rate, which is assumed for simplicity to be the one of Earth ($\Omega = 7.29 \cdot 10^{-5}$ rad.s^{-1}). All cases addressed in this study feature super-critical conditions for dynamo action at the beginning of the evolution and a high magnetic Reynolds number. A magnetic field shuts off if the inner core grows up to the outer core radius (see Section 4.1), if the convective velocity v is too low, or if the CMB heat flow is lower the heat conducted along the adiabat in the absence of inner core growth (chemical dynamos are viable otherwise). We define the lifetime of the magnetic field as the time interval in a planet's history during which the magnetic moment is non-zero. We do not consider sporadic field reactivations in the aftermath of the magnetic field shutting off in our lifetime calculations.

3 Results

3.1 Initial core structures

Hereafter we present results for core structures at the end of accretion, after the crystallisation of the silicates at the CMB. These are calculated using the model CHIC, described in Section 2.1.

Figure 2 shows internal structures (solid inner core, liquid outer core, silicate mantle) for planets of different mass and iron contents in the aftermath of accretion. It can clearly be seen that planets with higher bulk and mantle iron inventories feature larger cores and solid inner cores, which can even result in mostly or fully solid cores. Such large inner cores are a result of the increased internal pressures and densities of iron-rich planets, which raise the core melting temperature $T_\mathrm{m,core}$ (Equation (2)). Note that even though inner (and outer) core sizes increase for larger bulk iron inventories, planetary radii are smaller because of the higher core mass fraction, as shown in Figure 2. The size of the solid inner core corresponds to the radius at which the temperature matches the core melting temperature in Equation (2), calculated for a given pressure range and light element content x. Figure 3 shows the inner core radius fraction ($r_\mathrm{IC}/r_\mathrm{OC}$) at the end of accretion for the whole range of explored parameters. Plots are shown for cores made of pure iron (left column), and for cores containing iron and 5% of light elements (right column). The upper and lower row comprise cases with mantle iron numbers $\#Fe_\mathrm{M}$ of 0 and 0.1, respectively.

We find that planets with cores made of pure iron and low mantle iron numbers (e.g., upper left panel in Figure 3) do not feature solid inner cores if the bulk iron content is smaller than $X_\mathrm{Fe} \sim 35$ wt.%, regardless of the planetary mass. Above this threshold, early inner cores are present and can reach up to $>$ 80% of the core radius. The addition of 5% of light elements (Figure 3; right column) depresses the core melting temperature and pushes the presence of a solid inner core to higher bulk iron contents. A different distribution of iron between core and mantle influences the inner core size as well. As expected, planets with more iron in the mantle (i.e., a higher mantle iron number) have smaller core sizes, but solid inner cores tend to occupy a larger volume (see

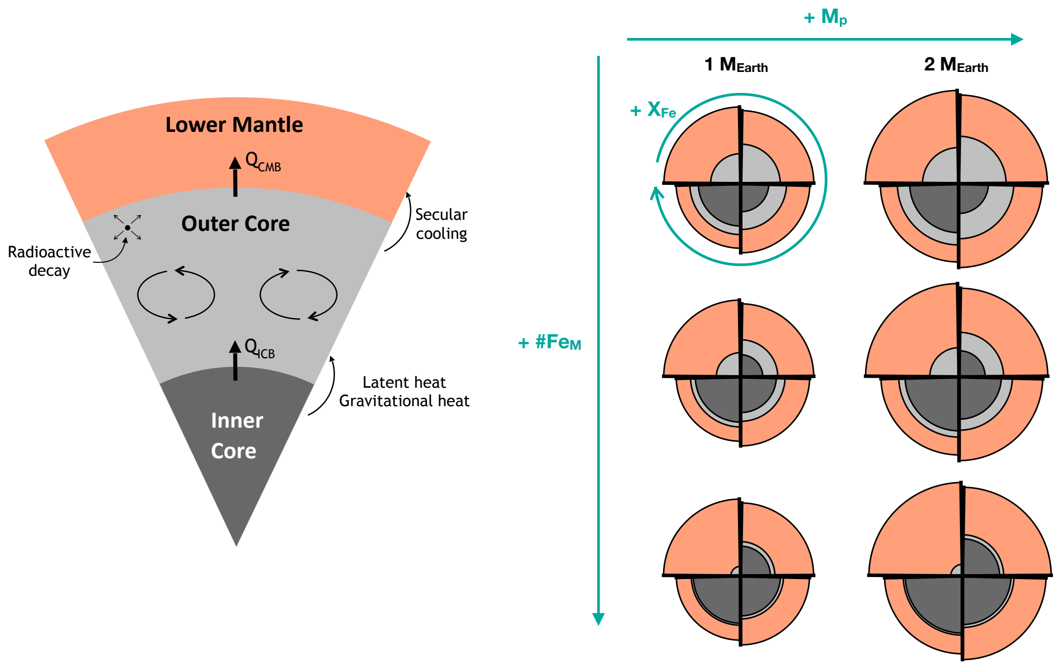

Figure 2. (Left) Schematic representation of a planetary interior showing the solid inner core, the liquid outer core, and a portion of the viscous lower mantle. As the inner core solidifies, it releases heat into the outer core in the form of latent and gravitational heat. In turn, the outer core releases heat into the mantle due to secular cooling. All these energy contributions drive convection in the outer core and power dynamo activity. (Right) Internal structures calculated for planets with different masses M_{p} (1 and 2 M_{Earth}) and iron contents in their early evolution stage, right after the crystallisation of molten silicates at the CMB. From top to bottom, the mantle iron number $\#Fe_{\mathrm{M}}$ is 0, 0.1, and 0.2. The bulk iron inventory X_{Fe} increases in clockwise direction (15, 35, 55, and 75 wt.% Fe in the upper left, upper right, lower right, and lower left quarters, respectively).

Figures 2 and 3). This is a result of the reduction of the mantle liquidus, which in turn leads to lower temperatures at the CMB and at the planetary centre (see Figure 1). An additional effect of higher mantle iron contents is the drastic increase of the mantle viscosity, which in turn reduces the efficiency of convection. As a result, heat is transported less efficiently from the core to the mantle, and a lower CMB heat flow is expected. Importantly, we note that the inner core fractions and radii (latter not shown) do not seem to be strongly dependent on the planetary mass. Instead, the iron inventory, the distribution of iron between core and mantle, and the light element content are the main controlling parameters.

3.2 Core evolution

Starting from planetary interior structures in the aftermath of accretion (see Sections 2.1 and 3.1), we investigate the evolution of the core using a parameterized thermal and magnetic evolution model (Section 2.2). Hereafter, we present some core evolution results for planets with masses of 1 and 2 M_{Earth} and bulk iron contents of 30 and 60 wt.% (see Figure 4). The core is made of iron and 5% light elements, and the mantle iron number $\#Fe_{\mathrm{M}}$ is set to zero. General trends summarising the outcomes of more simulations are shown in Section 3.3.

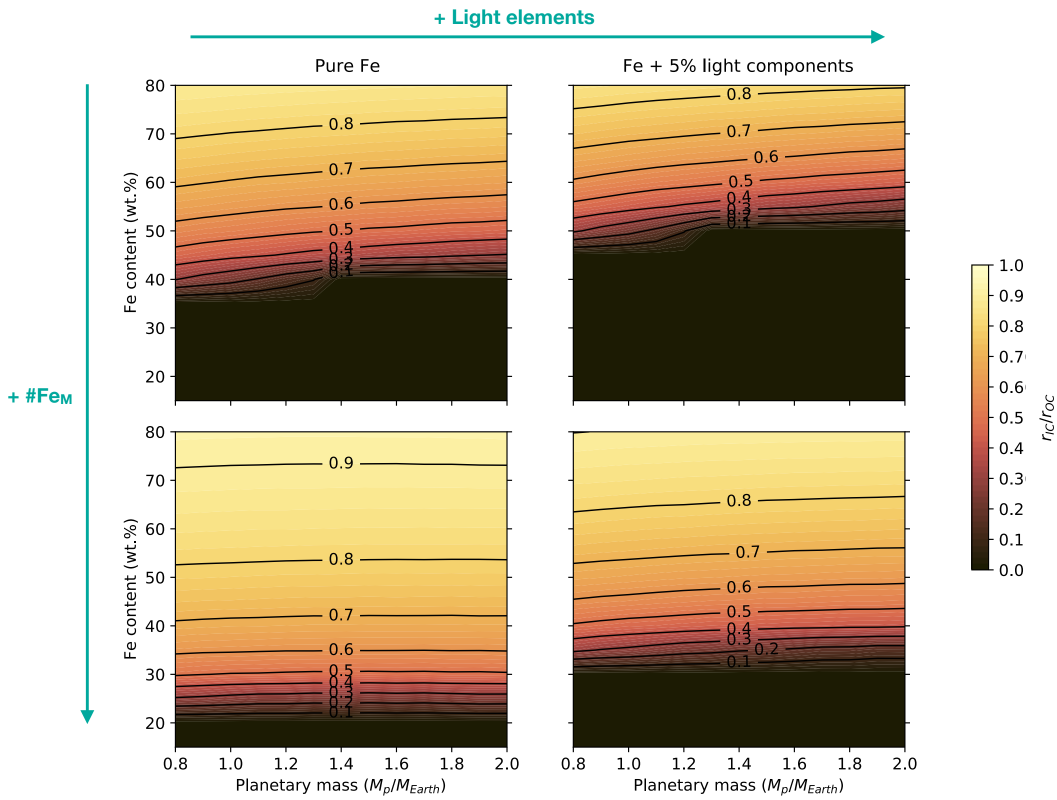

Figure 3. Radial fraction of the inner core ($r_{\mathrm{IC}}/r_{\mathrm{OC}}$) at the end of accretion as a function of planetary mass, bulk iron content, mantle iron number (upper row: $\#Fe_{\mathrm{M}} = 0$, lower row: $\#Fe_{\mathrm{M}} = 0.1$), and core composition (left column: pure iron, right column: iron and 5% light elements).

Inner core growth Figure 4A and B show the growth of the inner core during 5 Gyr, along with the temperature evolution at the CMB, for planets of 1 and 2 M_{Earth} with different iron contents (30 wt.% and 60 wt.%) and $\#Fe_{\mathrm{M}} = 0$, for a core containing iron and 5% of light elements. In contrast to iron-rich bodies, planets with a reduced bulk iron content (30 wt.% in Figure 4) display smaller core mass fractions (see also Figures 2 and 3) and tend to feature fully liquid cores in the aftermath of accretion. As soon as the temperature at the planetary centre reaches the melting temperature, an inner core starts growing as $r_{\mathrm{IC}}(t) \propto \sqrt{t}$ (Labrosse, 2003, 2015). In this scenario, the inner core growth curve is steeper in the early crystallisation stages due to the faster cooling of the planet, and flattens out later on. Planets with a higher bulk iron content, on the other hand, already start partially solid cores (e.g., $\sim 50\%$ of the core is solid for planets with 60 wt.% Fe in Figure 4). Despite the large difference in mass, 1 M_{Earth} planets tend to feature larger inner cores at the end of evolution compared to 2 M_{Earth} bodies. This is a result of the melting temperature slope flattening out at higher pressures, as shown in Figure 1. For all cases shown in Figure 4A, the solid inner core does not reach the outer core radius at the end of evolution, but we will show later in Section 3.3 that a large number of the analysed bodies end up with fully solid cores after 5 Gyr.

The temperature at the CMB lies on the adiabatic profile. Before an inner core starts crystallising, the profile is anchored to the central temperature, which is then shifted to the temperature at the ICB (assumed to be equal to the crystallisation temperature at

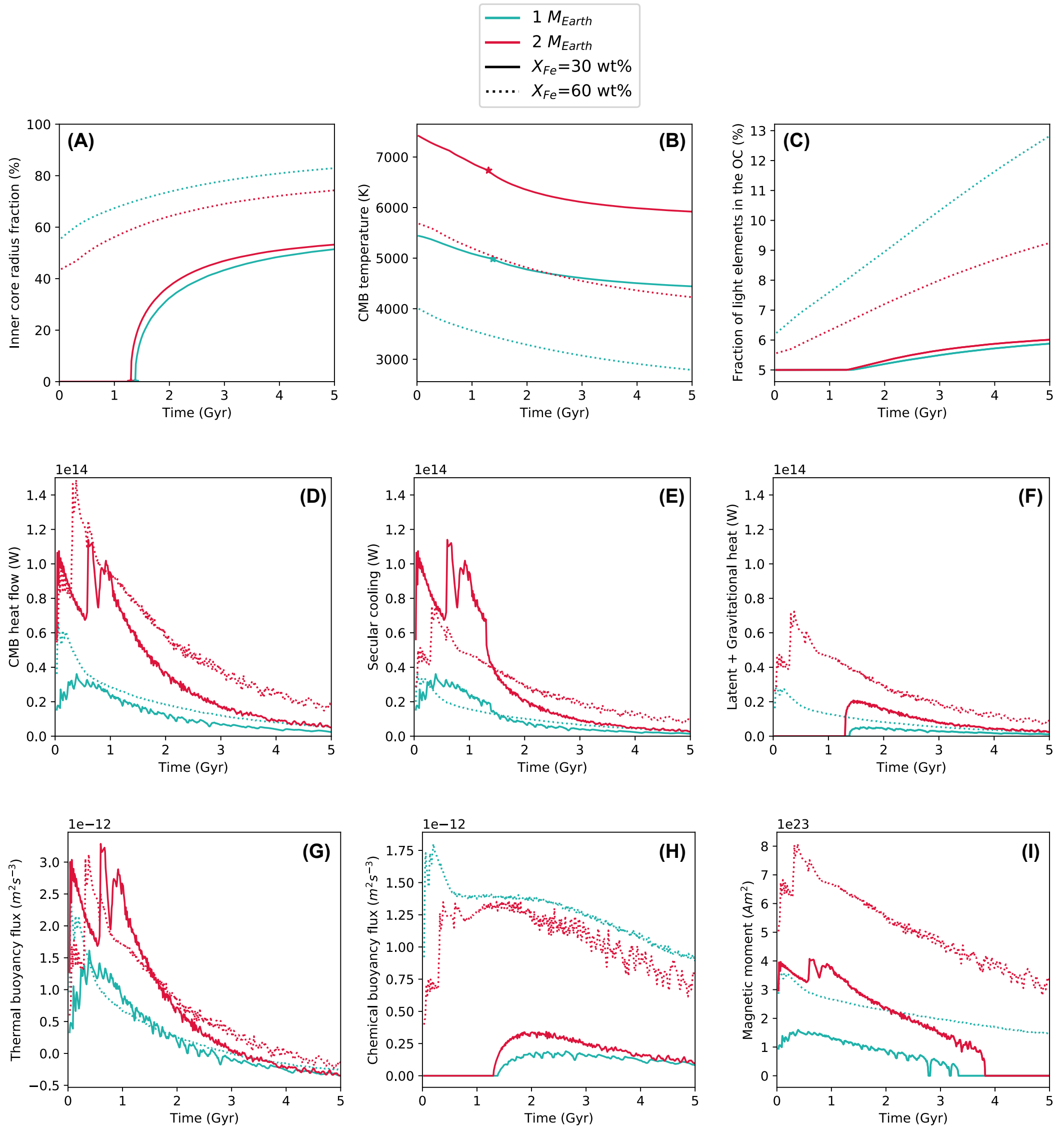

Figure 4. Evolution of the core during 5 Gyr for planets of 1 and 2 M_{Earth} with a bulk iron content of 30 and 60 wt.% and a mantle iron number $\#Fe_{\mathrm{M}}$ of 0. The core is made of pure iron and 5% of light elements. The different panels show: **(A)** Inner core radius fraction. **(B)** CMB temperature. The stars mark the inner core crystallisation onset. **(C)** Light element fraction in the liquid outer core (OC). **(D)** CMB heat flow for a stagnant-lid mantle. **(E)** Energy released from secular cooling. **(F)** Energy released from latent heat and gravitational heat. **(G)** Thermal buoyancy flux. **(H)** Chemical buoyancy flux. **(I)**Magnetic moment. As a reference, Earth's present-day magnetic moment is $7.8 \cdot 10^{22}$ Am^2.

that pressure) once an inner core starts forming (marked by a star in Figure 4A and B). As a result, the CMB temperature is higher for planets that start with no solid inner cores.

Light elements in the outer core As the solid inner core crystallises, the volume of the liquid outer core shrinks and becomes gradually enriched with light impurities, as shown in Figure 4C. We assume that these impurities are preferentially partitioned into the liquid phase. In the scenarios explored in Figure 4, the core has a bulk amount of light elements of 5%. However, depending on the size of the solid inner core (if any), the initial light element content in the outer core will differ. Following the examples shown in Figure 4, a 1 $M_{\rm Earth}$ planet containing 60 wt.% of iron will start with an inner core radius fraction of $\sim$ 55% (Figure 4A) and $\sim$ 6.3% of light elements in the outer core (Figure 4C). Instead, a body of same mass but containing 30 wt.% of iron will feature 5% of impurities in its fully liquid core. Due to the smaller inner core mass fraction of iron-poor bodies, the light element content in the liquid outer core will only increase by about $\sim$ 0.5% during evolution. On the other hand, bodies containing 60 wt.% of iron can grow large inner cores reaching up to $\sim$ 80% of the core radius, featuring thin liquid cores containing more than 10% of light components. The light element content in the liquid portion of the core has strong implications on the chemical composition of the latter with respect to the eutectic, as well as on the presence of different core formation mechanisms, as will be pointed out on the Discussion (Section 4.2).

Energy budget Figure 4D shows the evolution with time of the contributions to the energy budget for CMB heat flow histories for stagnant lid planets, calculated using the code CHIC (see Section 2.1.4 and Noack et al. (2017)). In the absence of an inner core, the CMB heat flow needs to be higher than the adiabatic one for thermal dynamo action to be viable. Once an inner core starts forming, a chemical dynamo can still take place even if the CMB heat flow lies below the adiabatic one. In the absence of heat supplied by radioactive decay, before an inner core starts forming, the only energy contribution to the CMB heat flow is provided by the secular cooling term as shown in Figure 4E (see also Section 2.2). Once an inner core starts crystallising, latent heat and gravitational energy (Figure 4F) start contributing as well, albeit being around one order of magnitude smaller than secular cooling.

More massive planets display higher CMB heat flows, resulting in higher secular cooling, latent, and gravitational heat terms. Despite having similar shapes, the CMB heat flow curves are all characterised by sharp oscillations during the first $\sim$ 1 Gyr of evolution. Such oscillations are the result of the initially very hot interior, triggering large-scale convective overturns not unsimilar to those seen in magma ocean crystallisation studies (Ballmer et al., 2017; Maurice et al., 2017). At later evolution stages CMB heat flows then partially converge to becoming smoother, although oscillations are still possible due to small-scale convection.

Buoyancy fluxes The evolution of the buoyancy fluxes is shown in panels G and H in Figure 4, for fluxes arising as a result of thermal and chemical anomalies. As a planet cools, thermally-generated buoyancy decays. The spikes in the thermal buoyancy flux curve reproduce the ones observed in the CMB heat flow evolution plot, as thermal buoyancy is proportional to the amount of heat extracted from the mantle.

Chemical buoyancy is driven by the release of light elements into the outer core after the onset of crystallisation of a solid inner core. The extent of chemical buoyancy is largely determined by the density jump at the ICB $\Delta\rho_{\rm ICB}$, which in turn depends on the amount of light elements present in the liquid outer core. As the outer core gradually becomes enriched in light components due to inner core crystallisation, the density jump at the ICB increases accordingly. Nevertheless, chemical buoyancy decays in time as a result of the smaller inner core growth rate ($dr_{\rm IC}/dt$, see Equation (23)) and drops to zero once the eutectic composition is reached.

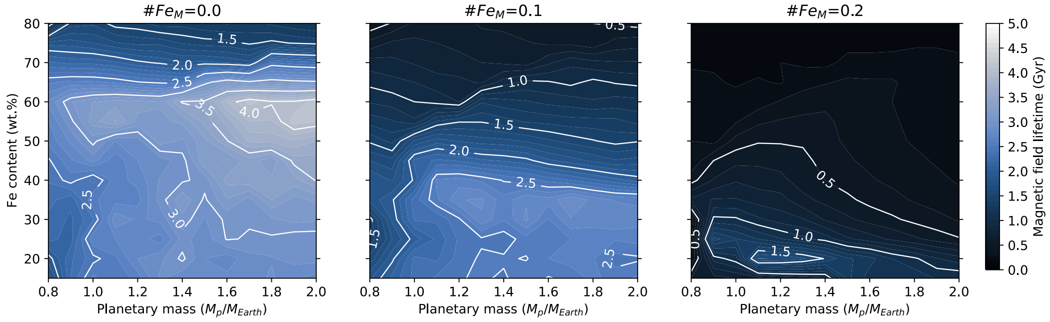

Figure 5. Magnetic field lifetimes for planets with different masses and bulk iron contents. Each panel comprises bodies with a different mantle iron number ($\#Fe_{\rm M} = 0 - 0.2$). The core is made of pure iron.

Magnetic field The dipolar magnetic moment is calculated using the scaling law by Olson and Christensen (2006) (Equation (25)). Its evolution is shown in Figure 4I for planets with different masses and iron contents. As outlined in Section 2.5, magnetic activity can take place if the magnetic Reynolds number is higher than a critical value of 40 and if the core is not entirely solid. The magnetic field also shuts off if the CMB heat flow is smaller than the heat conducted along the isentrope in the absence of inner core growth, as the existence of chemical dynamos is possible once an inner core starts forming. We find that the field is strongest, and magnetic activity lasts longer (with lifetimes reaching up to or more than ~ 5 Gyr) for massive and iron-rich planets. This is a result of their larger core sizes, as well as of the stronger CMB heat flow and resulting buoyancy fluxes. On the other hand, planets that are more iron-poor (i.e., 30 wt.% as shown in Figure 4) tend to have shorter-lived magnetic fields, with lifetimes of up to $\sim$ 3.8 Gyr. After the magnetic field shuts off, there may be some sporadic field reactivation episodes (see Figure 4I for a planet of 1 $M_{\rm Earth}$ and 30 wt.% of iron), resulting from the oscillatory behaviour of the CMB heat flow and the thermal and chemical buoyancy fluxes. While these episodes might be common in a planet's history, we do not take them into account when calculating the magnetic field lifetimes.

3.3 Magnetic field lifetimes and strengths

Hereafter, we present results exploring the full range of parameters introduced in this study. We focus on the evolution of the magnetic field, which is represented by its lifetime and maximum strength at the planetary surface. Results are shown as regime diagrams, with linear interpolations between the explored simulation cases.

Figure 5 shows the magnetic field lifetimes obtained for planets with different masses and iron contents (bulk and mantle) for cores made of pure iron. Magnetic field lifetimes are longest (~ 4.15 Gyr) for planets with higher mass, due to their elevated heat flows at the CMB. However, more than the planetary mass, the planetary iron content and distribution impact the lifetime of the magnetic field significantly. In this regard, we find that for each planetary mass the magnetic field lifetimes tend to increase up to intermediate bulk iron contents (~ 55 wt.% Fe), beyond which they start decaying. As inner cores of iron-rich planets occupy a larger fraction ($> 50\%$) of the core radius already at the beginning of evolution (i.e., in the aftermath of accretion), they require less time to reach the CMB and shut down any pre-existing magnetic activity. Similarly, an increase in the mantle iron inventory strongly shortens the time span during which magnetic activity takes place, with longest lifetime estimates being ~ 2.7 Gyr and ~ 1.5 Gyr for planets with mantle iron numbers $\#Fe_{\rm M}$ of 0.1 and 0.2, respectively. This is again

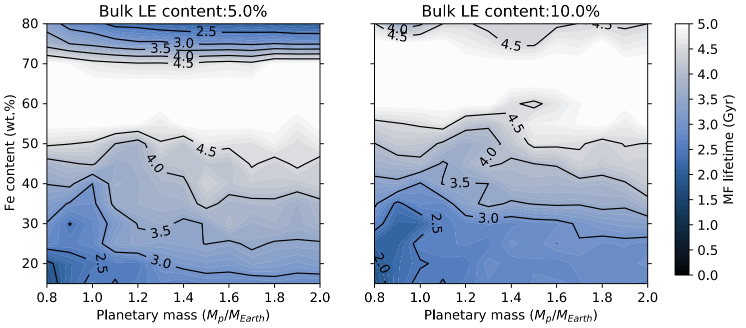

Figure 6. Magnetic field lifetimes for planets with different masses and bulk iron contents. The core is made of iron and 5 % (left panel) or 10 % (right panel) of light elements. The mantle iron number is $\#Fe_{\mathrm{M}} = 0$. The white regions denote parameter combinations for which the magnetic field is still active at the end of the simulations (and thus equals to 5 Gyr; see colorbar).

a result of the large inner core sizes arising from the depression of the mantle melting temperature, as depicted in Figure 1. Rocky planets that are both very rich in iron and/or have large mantle iron fractions are thus likely to have completely solid inner cores (see Figure S1 in the Supplementary Information), and no magnetic activity after 5 Gyr.

This scenario changes if the core is not made uniquely of iron, but contains a fraction of light elements. The lower melting temperatures cause inner cores to be smaller in size and delay the onset of inner core crystallisation. As a result, the longest magnetic field lifetimes (> 5 Gyr) are shifted towards higher iron inventories (Figure 6). Nevertheless, for bodies with large amounts of light elements (e.g., 10%) inner core crystallisation could be delayed to an extent at which thermal buoyancy alone is not able to sustain any magnetic activity anymore, leading to the extinction of the field.

Figure 7 shows the temporal maximum dipole field intensity at the planetary surface, obtained for planets with different masses and iron contents (bulk and mantle) for a core made of pure iron. The field intensity at the planetary surface B_{surf} scales from the intensity at the CMB B_{CMB} as $B_{\mathrm{surf}} = B_{\mathrm{CMB}}(r_{\mathrm{OC}}/r_{\mathrm{planet}})^3$ (where r_{planet} is the planetary radius), and thus strongly decreases for large planets with small core mass fractions. In addition, this quantity is proportional to the heat flow at the CMB, which governs the magnitude of thermal buoyancy fluxes, and is therefore expected to be highest during the early stages of a planet's evolution, similar to what is shown in Figure 4I for the dipole moment. The surface intensity is also important to assess the potential detectability of the generated magnetic fields (Section 4.5). We obtain the highest surface field intensities ($\sim 280\ \mu$T, about nine times stronger than the one at present-day Earth's surface) for massive planets with high bulk iron contents and low fractions of mantle iron. Therefore, despite displaying shorter-lived magnetic fields, as shown in Figure 5, planets that are very iron-rich (> 70 wt.% Fe) are expected to sustain a stronger magnetic field signatures during their early evolution. The addition of light components to the core increases chemical buoyancy fluxes, which in turn leads to an increase of the magnetic dipole moment and intensity at the surface up to $\sim 700\ \mu$T (see Figure 8).

Figure 9 summarises our results by showing the calculated planetary radii (Noack & Lasbleis, 2020), as well as the magnetic field lifetimes for planets with different masses and mantle iron numbers $\#Fe_{\mathrm{M}}$ for a core made of pure iron. Together with the planetary mass, the planetary radius is one of the observables for exoplanets, and is used here as a proxy for the bulk iron content, with larger radii indicating a lower iron inventory. Our results indicate that both a planet's iron content and the distribution of iron between the mantle and the core (and the planetary mass to a lesser extent) have strong

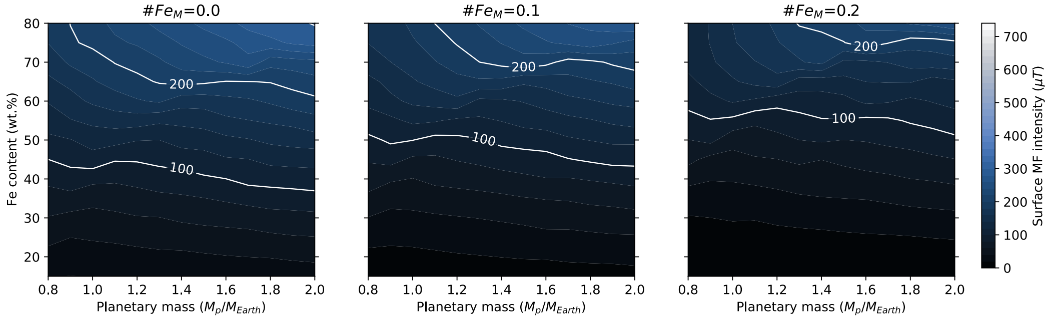

Figure 7. Temporal maximum magnetic field intensity at the planetary surface (as a reference, Earth's present-day surface intensity field is 30 μT). Each panel comprises bodies with a different mantle iron number. The core is made of pure iron.

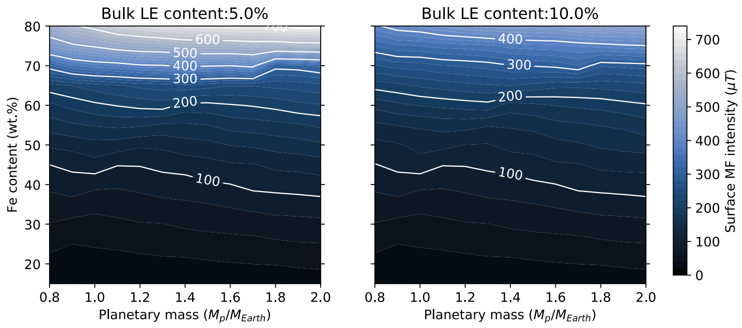

Figure 8. Temporal maximum magnetic field intensity at the planetary surface (as a reference, Earth's present-day surface intensity field is 30 μT). The mantle iron number Fe_{M} is 0 and the core is made of iron and 5% of light elements.

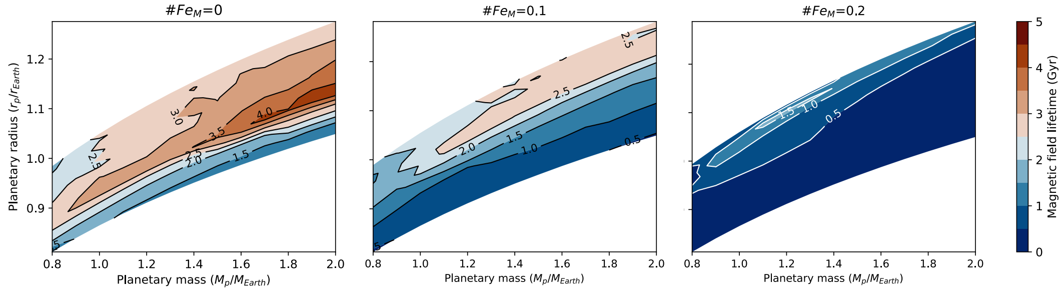

Figure 9. Magnetic field lifetimes obtained for planets with different masses, bulk iron contents, and mantle iron numbers $\#Fe_{\mathrm{M}}$. The core is made of pure iron. The planetary radii are calculated using the profiles in Noack and Lasbleis (2020). Note that the different mantle iron numbers in the three panels lead to different planetary radii.

implications for the lifetime of the magnetic field. This also confirms that mass and radius alone are not enough for constraining planetary internal structures, dynamics, and magnetic field features. Understanding the interaction of internally-generated magnetic fields with the atmosphere will open new avenues for constraining interior properties starting from atmospheric observations.

4 Discussion

4.1 Implications of large inner cores

During the course of evolution, a large portion of the analysed cores becomes completely or mostly solid. In the former case, the inner core has grown up to the size of the liquid outer core, while in the latter case the core consists of a large solid inner core and a thin convective shell. Besides having dramatic consequences for the existence of a magnetic field, this scenario can also have strong implications for dynamo morphology and for the pattern of convection in the remaining liquid. Figure 10 shows the time required for the solid inner core to reach 70% of the outer core radius, for planets of 1 and 2 M_{Earth} with different bulk and mantle iron contents (the core is made of pure iron). Since bodies with high mantle iron numbers tend to start their evolution with larger inner cores, the time elapsed until the outer core radius is reached is substantially reduced. As an example, 1 M_{Earth} planet having a bulk iron content of 15 wt.% and a mantle iron number $\#Fe_{\mathrm{M}} = 0$ needs much more than 5 Gyr for its core to become 70% solid, whereas it takes only ~ 2.7 Gyr for the same planet with a mantle iron number of 0.2. This is even more extreme for 2 M_{Earth} planets, for which the time is reduced to less than 1 Gyr for a high mantle iron number. The time required to reach a solid core fraction of 70% can be increased by a larger light element content.

Several studies have investigated dynamo morphology at different inner core fractions. Heimpel et al. (2005) examined the power spectra for dynamos at different shell geometries. They showed for inner core fractions lying between $r_{\mathrm{IC}}/r_{\mathrm{OC}} = 0.15{-}0.65$, the dipole energy increases up to $r_{\mathrm{IC}}/r_{\mathrm{OC}} = 0.45$. Above this threshold, the dipole energy slowly decays and the octupole and quadrupole contributions gradually increase. The importance of non-dipolar components has also been found by Takahashi and Matsushima (2006), who investigated convection in a thin shell with the inner core occupying 70% of the core radius. Based on similar findings, Stanley et al. (2007) suggested that a high octupole contribution might hint to the presence of a large inner core, whereas dipolar configurations might be a signature of small (Earth-like) solid inner cores. A change in the magnetic field morphology can have effects on the potential detectability of the

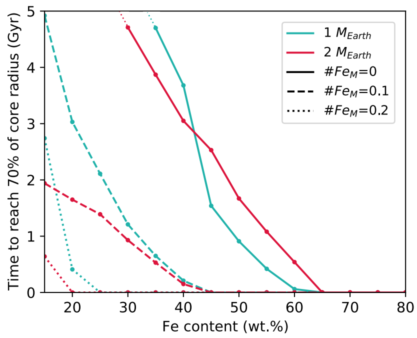

Figure 10. Time required for the solid inner core to reach 70% of the core radius as a function of bulk iron content X_{Fe}, for planets with mass 1 and 2 M_{Earth} and different iron numbers $\#Fe_{\mathrm{M}}$. The core is made of pure iron. Points for planets with low iron contents (bulk and mantle) are not shown, since the inner core never reaches 70% of the core radius.

field, with higher order configurations remaining more enclosed in the planetary interior and not manifesting at the surface.

Large inner cores can also influence the dynamics in the remaining thin liquid shell. With the Rayleigh number Ra being related to the shell thickness D_{shell} as $Ra \propto D^3_{\mathrm{shell}}$, the presence of a thin liquid outer core volume will likely lead to a smaller Rayleigh number, and hence to less vigorous convection. The resulting convective pattern, taking place in a region with a wide aspect ratio of horizontal and vertical scales of convection might be described by a different set of equations than the ones used here. A thin liquid layer can also affect flows powering the magnetic field. For cases with a small or absent inner core, magnetic activity is powered by large-scale columnar flows acting over the whole volume of the liquid outer core. In presence of a thin shell, these columnar flows might shift to smaller scales, which in turn might alter the strength and the long-term stability of the magnetic field.

While the dynamo configuration and outer core dynamics might be influenced by a large inner core to a certain extent, it is still unclear at which inner core radius this starts to happen, and thus needs further investigation. Nevertheless, we note that once inner cores become very large in our models, the equations employed here might not be adequate to describe the dynamics at that stage.

4.2 Composition of the outer core

As the inner core grows, the density and the composition of the outer core change due to the addition of light elements expelled from the solid inner core (here we assume that light components strongly partition into the liquid phase). The identity and abundance of light impurities in exoplanetary cores are unconstrained, mainly due to their high pressure conditions, which are challenging for mineral physics experiments and ab initio studies to reproduce. In our simulations we consider cores with bulk light element abundances of up to 10 wt.%. However, in the presence of large solid inner cores, light element fractions in the outer core can be substantially higher. Figure 11 shows light element abundances in the outer core after 5 Gyr of evolution for 5% and 10% bulk light element abundances, for planets of different mass and iron content. Planets with a smaller light element inventory (i.e., 5%; left panel of Figure 11) tend to grow larger (and earlier) solid inner cores than planets with more light elements in their cores. As a result, the outer core becomes more enriched in light components compared to bodies with a

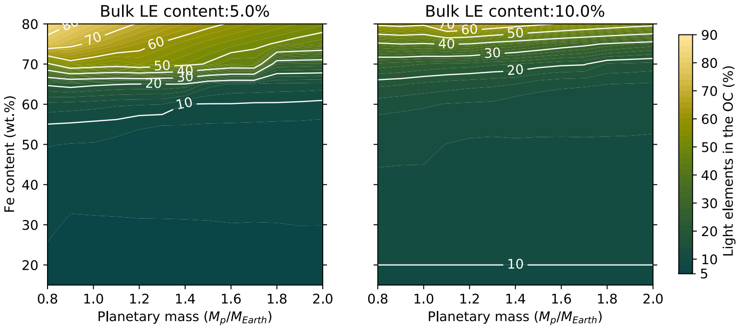

Figure 11. Fraction of light elements in the liquid outer core (OC) after 5 Gyr of evolution, as a function of planetary mass and bulk iron content. The left and right panel show fractions resulting from cores starting with bulk light element (LE) contents of 5% and 10%. We assume that light components are strongly partitioned into the liquid phase. The iron number $\#Fe_{\mathrm{M}}$ is 0 for all cases.

larger bulk amounts of light elements (e.g., 10%; right panel of Figure 11), with fractions reaching up to $X \sim 90\%$.

At such high light element contents, the outer core composition might lie at or beyond the eutectic point, on the iron-poor side of the phase diagram. This could imply the occurrence of different processes responsible for core crystallisation. For example, if the eutectic point is reached, two different phases start freezing, namely hpc-Fe and a light alloy FeX, where X is a light element (Braginsky, 1963). Such a mechanism will modify the energy balance in a way that is beyond the scope of the present study. In an attempt to simulate the attainment of the eutectic point, we topped the melting temperature depression to a maximum value of $\Delta T_{\mathrm{melt,core}} = 1500$ K, as proposed by Morard et al. (2011), beyond which outer core composition is kept to a pressure-dependent "eutectic" value and $\Delta\rho_{\mathrm{ICB}} = 0$. However, while our approach somewhat simulates the core reaching a eutectic, it is important to note that eutectic compositions for different alloys at conditions similar to the ones of super-Earths need further investigation.

4.3 Influence of the CMB heat flow history and of the initial thermal profiles

The CMB heat flow histories employed in this work are calculated using the code CHIC (Noack et al., 2017) for planets in a stagnant lid tectonic configuration. We acknowledge that the use of CMB heat flow histories for stagnant lid planets does not reproduce the thermal and magnetic history of Earth's core. Nevertheless, our core evolution model is based on the one by Labrosse (2015) and using a similar CMB heat flow history to the one employed there would lead to an evolution similar to Earth. The presence of a single stagnant ductile lithospheric plate acts as a cap and reduces the amount of heat that is released at the planetary surface. As a result, the heat flow at the CMB will be lower than for bodies featuring mobile lid-like mechanisms, which are expected to cool down at a faster rate. A similar effect might be exerted by the presence of an overlying thick atmospheres or a gaseous envelope (Lopez & Fortney, 2014; Weiss & Marcy, 2014), both of which can maintain the planetary interior hot. The role exerted by planetary atmospheres on the evolution of planetary cores and magnetic fields needs to be addressed by future work.

A further underestimation of the CMB heat flow is related to the fact that the input of latent and gravitational heat released from the growth of an inner core are not taken into account in the mantle evolution model employed to obtain the CMB heat flow histories (see also Section 2.1.4). The coupling between mantle and core evolution is thus needed. However, for this study we employ a hot initial thermal profile, which is an upper limit of the profile in Stixrude (2014). In this scenario, the CMB temperature is anchored to the mantle liquidus, which leads to an initially hot core. This may, in turn, promote higher CMB heat flows compared to the ones obtained in previous work (Valencia et al., 2006; Tackley et al., 2013).

In order to compare our results with other thermal profiles, we ran the evolution models for bodies with a warm initial temperature profile, which corresponds to the case described in Stixrude (2014) and to the warm case in Noack and Lasbleis (2020). In this scenario, the temperature at the CMB is anchored to the mantle solidus. Hot and warm initial thermal profiles can represent different stages in a planet's evolution, as well as a different thickness of the overlying atmosphere, if any (Hamano et al., 2013). In this regard, a hot initial profile would be indicative of a planet surrounded by a thick insulating atmosphere, which would delay mantle freezing and lead to a long-lived magma ocean. On the other hand, a warm initial profile would represent a planet short-lived magma ocean and a thinner atmosphere.

Starting out from a warm internal profile implies lower heat flows at the CMB, as well as cores that are partially or entirely solid. We find that regardless of the iron content (bulk and mantle) all cores end up being completely solid after 5 Gyr of evolution. As a result, the magnetic field lifetime is drastically reduced and reaches values slightly higher than 3 Gyr for a mantle iron number $\#Fe_{\mathrm{M}} = 0$ and low bulk iron contents ($<$ 20 wt.%). The presence of light impurities can help maintaining the field for longer, although lifetimes are still shorter than what obtained for the hot temperature scenario.

4.4 Influence of the thermal conductivity

The lifetime of a magnetic field is also highly dependent on the core thermal conductivity, which determines how fast heat is conducted to the mantle. A number of recent findings reporting higher thermal conductivities than previously thought (Pozzo et al., 2012; Gomi et al., 2013) have dramatically challenged the current understanding of processes taking place in the cores of Earth and other planets. Other processes enabling a longer-lived dynamo action have since then been invoked (ORourke & Stevenson, 2016; Hirose et al., 2017).

Thermal conductivities of super-Earths' cores are unknown and will likely be challenging to determine in the near future. As mentioned in the Methods section, we employ a thermal conductivity of 150 W.m^{-1}.K^{-1}, which lies in the upper range of estimates for Earth. For comparison, we ran core evolution simulations using thermal conductivities of 60 and 250 W.m^{-1}.K^{-1}. For cores made of pure iron, we obtain upper estimates of the magnetic field lifetime amounting to 5 Gyr for planets with a thermal conductivitiy of 60, and almost 2 Gyr lower (3.2 Gyr) for bodies having thermal conductivities of 250. Such upper estimates are obtained for mantle iron numbers of 0. The addition of light elements yields magnetic field lifetimes longer than 5 Gyr for 60 and of up to 4.43 Gyr for 250 W.m^{-1}.K^{-1}. The thermal conductivity remains a strongly controlling parameter and varying its value can thus significantly impact our results. Constraining this parameter for planets in our solar system like Mars, the Moon, and Mercury will help understanding how strong the thermal conductivity changes with pressure.

4.5 Detectability

Magnetic fields of planets in the solar system were first detected by measuring their radio electron cyclotron emission, which generates from the interaction between the stellar wind and the magnetised planet. These observations are carried out from the ground using radio telescopes such as the Low-Frequency Array (LOFAR) (Kassim et al., 2004). As a result, only signals with frequencies greater than 10 MHz (i.e., the ionospheric cutoff) are able to penetrate Earth's atmosphere and be detected. This constitutes a bias on the type of magnetic fields that can be observed, which are mainly on the order of the ones produced by giant planets like Jupiter and Saturn.

In order to be detectable, the magnetic field of a (exo)planet must fulfil two conditions: It must produce cyclotron emission signals with frequencies higher than the ionospheric cutoff of 10 MHz (and thus have a magnetic field surface intensity of $B_\mathrm{s} = 384$ μT), and have a flux density higher than the sensitivity of the instrument the observation is carried out with. The sensitivity describes the minimum signal that a telescope is able to detect within a given time frame. In their study, Driscoll and Olson (2011) have discussed the potential observability of exoplanetary magnetic fields through radio emissions, and we redirect the reader to that paper for more information on the relevant equations. While we explore a wider range of parameters (core mass fractions, iron distributions, and light element content), and despite some differences in the modelling approach (e.g., the use of different melting temperatures, CMB heat flow histories, and the consideration of chemical buoyancy), we find that the magnetic surface intensities obtained here (see Figure 7) match quite well with the ones discussed in Driscoll and Olson (2011) for planets of up to 2 M_Earth (see Figure 7). Planets with pure iron cores do not produce strong enough fields to emit at frequencies higher than the ionospheric cutoff, bodies with cores containing light impurities can reach surface field intensities of up to $\sim$ 650 μT. Such planets can attain electron cyclotron frequencies f_c of up to $\sim$ 18 MHz, above the ionospheric cutoff.

Planets can be detected if their flux density is higher than the one required by the LOFAR telescope. The flux density is related to a planet's distance from the solar system, its cutoff frequency, and its radio emission. The latter quantity depends on a planet's magnetic moment and its semi-major axis. Planets located in systems further away from the Sun will need to have smaller orbital distances in order to be detected. We find that planets located 1 pc away from the Sun are detectable only if they lie within $\sim 10^{-3}$ AU from their host star. This orbital distance is reduced to $\sim\ 2 \cdot 10^{-5}$ AU for bodies located 100 pc away from the solar system. At such small semi-major axes, rocky planets may not be in stable orbital configurations and are expected to spiral and collapse into the host star. It needs to be noted, however, that the radio emission of a planet also changes according to the stellar activity, which influences the intensity, density, and velocity of stellar winds. Sporadic energetic events such as coronal mass ejections can increase the flux density of the signal by $1{-}2$ orders of magnitude (Farrell et al., 1999), and planets located further away from the host star might become temporarily detectable. We conclude that even if exoplanetary cores contain light elements raising the magnetic field intensities, current specifications of radio telescopes such as LOFAR may be not sensitive enough to detect the emission generated by their magnetic fields. Nevertheless, the development of indirect observation techniques, such as UV and radio wave transits (Fossati et al., 2010; Withers & Vogt, 2017), can provide useful insights on planetary composition, interior structure and magnetic activity.

5 Summary and Conclusions

The presence of a magnetic field during a planet's history is thought to influence its evolution, as well as the development and long-term stability of habitable surface conditions. Magnetic fields of rocky bodies are generated in an electrically conductive liquid layer in their deep interior (the metallic molten outer core for Earth). The discovery of a large amount of exoplanets and the search for extraterrestrial life motivate the investigation of the evolution and diversity of exo-magnetic fields. This constitutes a challenging task, as interior properties of exoplanets are difficult to estimate from current data.

This work presents structures and evolution trends of the cores of a diverse set of planets with different masses (0.8−2 M_{Earth}), iron contents (indicated by the bulk iron fraction), as well as variable partitioning of iron between the mantle and core (indicated by the mantle iron number). We employ an interior structure model (Noack & Lasbleis, 2020) to obtain core structures at the late stages of planet formation and the evolution of the heat flow at the CMB. Starting from these, we model the subsequent thermal and magnetic evolutions of the cores, and calculate how long magnetic activity can be sustained. Our main findings are:

- While the planetary mass is not the most controlling parameter, the iron inventory strongly affects a planet's core thermal and magnetic evolution.
- The presence of a solid inner core is common among newly-formed planets with high bulk and/or high mantle iron contents displaying large solid inner cores, as a result of the higher core mass fraction and the lower mantle melting temperature. Cores containing small fractions of light elements start with smaller inner cores due to the depression of the core melting temperature exerted by the presence of light impurities.
- During 5 Gyr of evolution, a large portion of the analysed cores become mostly or fully solid. Solid inner cores occupying more than $\sim 70\%$ of the v olume of the core might be compatible with a lower dipole energy and different convection patterns, compared to cases with a smaller inner solid sphere. This can affect the generation and surface manifestation (detectability) of a magnetic field.
- The generated magnetic fields can remain active for up to ~ 4.2 Gyr, where longer lifetimes are obtained for planets with intermediate/high iron fractions (60−75 wt.%) and low mantle iron numbers. Lifetimes can be extended to 5 Gyr or longer in presence of a small fraction of core impurities. Planets that are more iron-rich tend to grow inner cores that quickly reach the CMB, shutting off any pre-existing magnetic activity, thus leading to shorter magnetic field lifetimes.
- The expulsion of light components to the liquid outer core as the solid inner core grows enriches the former with impurities, whose fraction can reach up to $\sim 90\%$ after 5 Gyr of evolution. Large light element contents may be compatible with the attainment of the eutectic (or cotectic). This may lead to different core crystallisation mechanisms, powering the magnetic field in a different way, not explored in this study.
- The calculated magnetic field surface intensities can reach up to ~ 700 μT, i.e. ~ 23 times the one of present-day Earth. Even though their signal lies above the ionospheric cutoff frequency of 10 MHz, their emitted flux is too weak to be detected by current ground-based radio telescopes. The use of different, indirect, observation strategies (spectroscopic transit observations, observations of planetary dust tails) could provide further insights and constraints on exoplanetary magnetism.

Investigating the diversity of exoplanetary magnetic fields will improve our understanding of the evolution of planets in our solar system and beyond. Ultimately, it is important to constrain the influence and feedback of internally generated magnetic fields on the planetary atmospheric evolution and habitability by fully coupling interior processes to ones at the outer edge of the atmosphere and the stellar environment. This will enable to constrain interior properties from future observed atmospheric parameters. This study provides a first step in this direction, by presenting some of the trends obtained from the evolution of exoplanetary cores.

Acknowledgments

This research has made use of the Exoplanet Orbit Database and the Exoplanet Data Explorer at exoplanets.org. IB acknowledges financial support from the Japanese Society for the Promotion of Science (JSPS). ML was funded by the European Union's Horizon 2020 research and innovation program under the Marie Skłodowska-Curie Grant Agreement No. 795289. LN acknowledges financial support from the German Research Foundation (DFG) for project NO 1324/6-1. IB and ML thank Guillaume Morard, John Hernlund and Hagay Amit for helpful discussions. The authors appreciate the support of ELSI, Tokyo, to host the Planetary Diversity Workshop in 2016, which initiated this study. LN would like to thank the HPC Service of ZEDAT, Freie Universität Berlin, for computing time. The simulations were analysed using the open source software environment Matplotlib (Hunter, 2007). Figures were generated using the perceptually uniform scientific colour maps lajolla, oslo, and bamako (Crameri, 2018) to prevent visual distortion. All codes or simulation results needed to reproduce the figures in this paper are available on Gitlab.

References

Abe, Y. (1997). Thermal and chemical evolution of the terrestrial magma ocean. *Physics of the Earth and Planetary Interiors*, *100*(1-4), 27–39.

Akeson, R., Chen, X., Ciardi, D., Crane, M., Good, J., Harbut, M., … others (2013). The nasa exoplanet archive: data and tools for exoplanet research. *Publications of the Astronomical Society of the Pacific*, *125*(930), 989.

Andrault, D., Bolfan-Casanova, N., Nigro, G. L., Bouhifd, M. A., Garbarino, G., & Mezouar, M. (2011). Solidus and liquidus profiles of chondritic mantle: Implication for melting of the earth across its history. *Earth and planetary science letters*, *304*(1-2), 251–259.

Aubert, J., Labrosse, S., & Poitou, C. (2009). Modelling the palaeo-evolution of the geodynamo. *Geophysical Journal International*, *179*(3), 1414–1428.

Badro, J., Brodholt, J. P., Piet, H., Siebert, J., & Ryerson, F. J. (2015). Core formation and core composition from coupled geochemical and geophysical constraints. *Proceedings of the National Academy of Sciences*, *112*(40), 12310–12314.

Ballmer, M. D., Lourenço, D. L., Hirose, K., Caracas, R., & Nomura, R. (2017). Reconciling magma-ocean crystallization models with the present-day structure of the earth's mantle. *Geochemistry, Geophysics, Geosystems*, *18*(7), 2785–2806.

Baraffe, I., Chabrier, G., Fortney, J., & Sotin, C. (2014). Planetary internal structures. *arXiv preprint arXiv:1401.4738*.

Bitsch, B., & Battistini, C. (2020). Influence of sub-and super-solar metallicities on the composition of solid planetary building blocks. *Astronomy & Astrophysics*, *633*, A10.

Bond, J. C., O'Brien, D. P., & Lauretta, D. S. (2010). The compositional diversity of extrasolar terrestrial planets. i. in situ simulations. *The Astrophysical Journal*, *715*(2), 1050.

Bouchet, J., Mazevet, S., Morard, G., Guyot, F., & Musella, R. (2013). Ab initio equation of state of iron up to 1500 gpa. *Physical Review B*, *87*(9), 094102.

Boujibar, A., Driscoll, P., & Fei, Y. (2020). Super-earth internal structures and initial thermal states. *Journal of Geophysical Research: Planets*, *125*(5), e2019JE006124.

Braginsky, S. (1963). Structure of the f layer and reasons for convection in the earth's core. In *Soviet phys. dokl.* (Vol. 149, pp. 8–10).

Braginsky, S., & Roberts, P. H. (1995). Equations governing convection in earth's core and the geodynamo. *Geophysical & Astrophysical Fluid Dynamics*, *79*(1-4), 1–97.

Brain, D., Leblanc, F., Luhmann, J., Moore, T. E., & Tian, F. (2013). Planetary magnetic fields and climate evolution. *cctp*, 487.

Breuer, D., Labrosse, S., & Spohn, T. (2010). Thermal evolution and magnetic field generation in terrestrial planets and satellites. *Space Science Reviews*, *152*(1-4), 449–500.

Buffett, B. A. (2003). The thermal state of earth's core. *Science*, *299*(5613), 1675–1677.

Canup, R. M. (2004). Dynamics of lunar formation. *Annu. Rev. Astron. Astrophys.*, *42*, 441–475.

Christensen, U. R., & Aubert, J. (2006). Scaling properties of convection-driven dynamos in rotating spherical shells and application to planetary magnetic fields. *Geophysical Journal International*, *166*(1), 97–114.

Crameri, F. (2018). Scientific colour-maps. *Zenodo*, *10*. doi: 10.5281/zenodo.3596401

Dehant, V., Lammer, H., Kulikov, Y. N., Grießmeier, J.-M., Breuer, D., Verhoeven, O., … Lognonné, P. (2007). Planetary magnetic dynamo effect on atmospheric protection of early earth and mars. *Space Science Reviews*, *129*(1-3), 279–300.

Del Genio, A. D., Brain, D., Noack, L., & Schaefer, L. (2020). The inner solar systems habitability through time. *Planetary Astrobiology*, 419.

Dorn, C., Harrison, J. H., Bonsor, A., & Hands, T. O. (2019). A new class of super-earths formed from high-temperature condensates: Hd219134 b, 55 cnc e, wasp-47 e. *Monthly Notices of the Royal Astronomical Society*, *484*(1), 712–727.

Dorn, C., Noack, L., & Rozel, A. (2018). Outgassing on stagnant-lid super-earths. *Astronomy & Astrophysics*, *614*, A18.

Driscoll, P., & Olson, P. (2011). Optimal dynamos in the cores of terrestrial exoplanets: Magnetic field generation and detectability. *Icarus*, *213*(1), 12–23.

Dumoulin, C., Tobie, G., Verhoeven, O., Rosenblatt, P., & Rambaux, N. (2017). Tidal constraints on the interior of venus. *Journal of Geophysical Research: Planets*, *122*(6), 1338–1352.

Elkins-Tanton, L. T., & Seager, S. (2008). Coreless terrestrial exoplanets. *The Astrophysical Journal*, *688*(1), 628.

Farrell, W., Desch, M., & Zarka, P. (1999). On the possibility of coherent cyclotron emission from extrasolar planets. *Journal of Geophysical Research: Planets*, *104*(E6), 14025–14032.

Fossati, L., Haswell, C., Froning, C., Hebb, L., Holmes, S., Kolb, U., … others (2010). Metals in the exosphere of the highly irradiated planet wasp-12b. *The Astrophysical Journal Letters*, *714*(2), L222.

Frank, E. A., Meyer, B. S., & Mojzsis, S. J. (2014). A radiogenic heating evolution model for cosmochemically earth-like exoplanets. *Icarus*, *243*, 274–286.

Gardner, J. P., Mather, J. C., Clampin, M., Doyon, R., Greenhouse, M. A., Hammel, H. B., … others (2006). The james webb space telescope. *Space Science Reviews*, *123*(4), 485–606.

Gomi, H., Ohta, K., Hirose, K., Labrosse, S., Caracas, R., Verstraete, M. J., & Hernlund, J. W. (2013). The high conductivity of iron and thermal evolution of the earths core. *Physics of the Earth and Planetary Interiors*, *224*, 88–103.

Gubbins, D. (1977). Energetics of the earth's core. *Journal of Geophysics-Zeitschrift f r Geophysik*, *43*(1), 453–464.

Hakim, K., Rivoldini, A., Van Hoolst, T., Cottenier, S., Jaeken, J., Chust, T., & Steinle-Neumann, G. (2018). A new ab initio equation of state of hcp-fe and its implication on the interior structure and mass-radius relations of rocky super-earths. *Icarus*, *313*, 61–78.

Hamano, K., Abe, Y., & Genda, H. (2013). Emergence of two types of terrestrial planet on solidification of magma ocean. *Nature*, *497*(7451), 607–610.

Hauck, S. A., Aurnou, J. M., & Dombard, A. J. (2006). Sulfur's impact on core evolution and magnetic field generation on ganymede. *Journal of Geophysical Research: Planets*, *111*(E9).

Heimpel, M., Aurnou, J., Al-Shamali, F., & Perez, N. G. (2005). A numerical study of dynamo action as a function of spherical shell geometry. *Earth and Planetary Science Letters*, *236*(1-2), 542–557.

Hernlund, J. W., & Tackley, P. J. (2008). Modeling mantle convection in the spherical annulus. *Physics of the Earth and Planetary Interiors*, *171*(1-4), 48–54.

Hirose, K., Labrosse, S., & Hernlund, J. (2013). Composition and state of the core. *Annual Review of Earth and Planetary Sciences*, *41*, 657–691.

Hirose, K., Morard, G., Sinmyo, R., Umemoto, K., Hernlund, J., Helffrich, G., & Labrosse, S. (2017). Crystallization of silicon dioxide and compositional evolution of the earths core. *Nature*, *543*(7643), 99–102.

Howe, A. R., Burrows, A., & Verne, W. (2014). Mass-radius relations and core-envelope decompositions of super-earths and sub-neptunes. *The Astrophysical Journal*, *787*(2), 173.

Huguet, L., Van Orman, J. A., Hauck II, S. A., & Willard, M. A. (2018). Earth's inner core nucleation paradox. *Earth and Planetary Science Letters*, *487*, 9–20.

Hunter, J. D. (2007). Matplotlib: A 2d graphics environment. *Computing in Science & Engineering*, *9*(3), 90–95. doi: 10.1109/MCSE.2007.55

Karato, S.-i., & Wu, P. (1993). Rheology of the upper mantle: A synthesis. *Science*, *260*(5109), 771–778.

Kassim, N., Lazio, T., Ray, P., Crane, P., Hicks, B., Stewart, K., … Lane, W. (2004). The low-frequency array (lofar): opening a new window on the universe. *Planetary and Space Science*, *52*(15), 1343–1349.

Konôpková, Z., McWilliams, R. S., Gómez-Pérez, N., & Goncharov, A. F. (2016). Direct measurement of thermal conductivity in solid iron at planetary core conditions. *Nature*, *534*(7605), 99–101.

Konopliv, A., & Yoder, C. (1996). Venusian k2 tidal love number from magellan and pvo tracking data. *Geophysical research letters*, *23*(14), 1857–1860.

Koper, K. D., & Pyle, M. L. (2004). Observations of pkikp/pcp amplitude ratios and implications for earth structure at the boundaries of the liquid core. *Journal of Geophysical Research: Solid Earth*, *109*(B3).

Kuchner, M. J., & Seager, S. (2005). Extrasolar carbon planets. *arXiv preprint astro-ph/0504214*.

Kuwayama, Y., & Hirose, K. (2004). Phase relations in the system fe-fesi at 21 gpa. *American Mineralogist*, *89*(2-3), 273–276.

Labrosse, S. (2003). Thermal and magnetic evolution of the earths core. *Physics of the Earth and Planetary Interiors*, *140*(1-3), 127–143.

Labrosse, S. (2015). Thermal evolution of the core with a high thermal conductivity. *Physics of the Earth and Planetary Interiors*, *247*, 36–55.

Labrosse, S., Hernlund, J., & Coltice, N. (2007). A crystallizing dense magma ocean at the base of the earths mantle. *Nature*, *450*(7171), 866–869.

Labrosse, S., Poirier, J.-P., & Le Mouël, J.-L. (2001). The age of the inner core. *Earth and Planetary Science Letters*, *190*(3-4), 111–123.

Lammer, H., Zerkle, A. L., Gebauer, S., Tosi, N., Noack, L., Scherf, M., … others (2018). Origin and evolution of the atmospheres of early venus, earth and mars. *The Astronomy and Astrophysics Review*, *26*(1), 2.

Lay, T., Hernlund, J., & Buffett, B. A. (2008). Core–mantle boundary heat flow. *Nature geoscience*, *1*(1), 25.

Lister, J. R., & Buffett, B. A. (1995). The strength and efficiency of thermal and compositional convection in the geodynamo. *Physics of the Earth and Planetary Interiors*, *91*(1-3), 17–30.

Lopez, E. D., & Fortney, J. J. (2014). Understanding the mass-radius relation for sub-neptunes: radius as a proxy for composition. *The Astrophysical Journal*, *792*(1), 1.

López-Morales, M., Gómez-Pérez, N., & Ruedas, T. (2011). Magnetic fields in earth-like exoplanets and implications for habitability around m-dwarfs. *Origins of*

Life and Evolution of Biospheres, *41*(6), 533–537.

Masters, G., & Gubbins, D. (2003). On the resolution of density within the earth. *Physics of the Earth and Planetary Interiors*, *140*(1-3), 159–167.

Maurice, M., Tosi, N., Samuel, H., Plesa, A.-C., Hüttig, C., & Breuer, D. (2017). Onset of solid-state mantle convection and mixing during magma ocean solidification. *Journal of Geophysical Research: Planets*, *122*(3), 577–598.

McDonough, W. F., & Sun, S.-S. (1995). The composition of the earth. *Chemical geology*, *120*(3-4), 223–253.

McIntyre, S. R., Lineweaver, C. H., & Ireland, M. J. (2019). Planetary magnetism as a parameter in exoplanet habitability. *Monthly Notices of the Royal Astronomical Society*, *485*(3), 3999–4012.

Monteux, J., Andrault, D., & Samuel, H. (2016). On the cooling of a deep terrestrial magma ocean. *Earth and Planetary Science Letters*, *448*, 140–149.

Moore, T. E., & Horwitz, J. (2007). Stellar ablation of planetary atmospheres. *Reviews of Geophysics*, *45*(3).

Moore, W. B., & Webb, A. A. G. (2013). Heat-pipe earth. *Nature*, *501*(7468), 501–505.

Morard, G., Andrault, D., Guignot, N., Sanloup, C., Mezouar, M., Petitgirard, S., & Fiquet, G. (2008). In situ determination of fe–fe3s phase diagram and liquid structural properties up to 65 gpa. *Earth and Planetary Science Letters*, *272*(3-4), 620–626.

Morard, G., Bouchet, J., Valencia, D., Mazevet, S., & Guyot, F. (2011). The melting curve of iron at extreme pressures: Implications for planetary cores. *High Energy Density Physics*, *7*(3), 141–144.

Moriarty, J., Madhusudhan, N., & Fischer, D. (2014). Chemistry in an evolving protoplanetary disk: effects on terrestrial planet composition. *The Astrophysical Journal*, *787*(1), 81.

Nakajima, M., & Stevenson, D. J. (2015). Melting and mixing states of the earth's mantle after the moon-forming impact. *Earth and Planetary Science Letters*, *427*, 286–295.

Nimmo, F. (2002). Why does venus lack a magnetic field? *Geology*, *30*(11), 987–990.

Nimmo, F. (2007). Energetics of the core. *Treatise on geophysics*, *8*, 31–65.

Noack, L., Godolt, M., von Paris, P., Plesa, A.-C., Stracke, B., Breuer, D., & Rauer, H. (2014). Can the interior structure influence the habitability of a rocky planet? *Planetary and Space Science*, *98*, 14–29.

Noack, L., & Lasbleis, M. (2020). Parameterisations of interior properties of rocky planets: Investigation of planets with earth-like compositions but variable iron content. *Astronomy & Astrophysics*.

Noack, L., Rivoldini, A., & Van Hoolst, T. (2017). Volcanism and outgassing of stagnant-lid planets: implications for the habitable zone. *Physics of the Earth and Planetary Interiors*, *269*, 40–57.

Nomura, R., Ozawa, H., Tateno, S., Hirose, K., Hernlund, J., Muto, S., … Hiraoka, N. (2011). Spin crossover and iron-rich silicate melt in the earths deep mantle. *Nature*, *473*(7346), 199–202.

Olson, P., & Christensen, U. R. (2006). Dipole moment scaling for convection-driven planetary dynamos. *Earth and Planetary Science Letters*, *250*(3-4), 561–571.

ONeill, C., Lenardic, A., Weller, M., Moresi, L., Quenette, S., & Zhang, S. (2016). A window for plate tectonics in terrestrial planet evolution? *Physics of the Earth and Planetary Interiors*, *255*, 80–92.

ORourke, J. G., & Stevenson, D. J. (2016). Powering earths dynamo with magnesium precipitation from the core. *Nature*, *529*(7586), 387–389.

Poirier, J.-P. (1994). Light elements in the earth's outer core: a critical review. *Physics of the earth and planetary interiors*, *85*(3-4), 319–337.

Pozzo, M., Davies, C., Gubbins, D., & Alfe, D. (2012). Thermal and electrical conductivity of iron at earths core conditions. *Nature*, *485*(7398), 355–358.

Roberts, P. (2015). Theory of the geodynamo. *Core Dynamics*, 67–105.

Rogers, L., & Seager, S. (2010). A framework for quantifying the degeneracies of exoplanet interior compositions. *The Astrophysical Journal*, *712*(2), 974.

Rubie, D. C., Frost, D. J., Mann, U., Asahara, Y., Nimmo, F., Tsuno, K., ... Palme, H. (2011). Heterogeneous accretion, composition and core–mantle differentiation of the earth. *Earth and Planetary Science Letters*, *301*(1-2), 31–42.

Rückriemen, T., Breuer, D., & Spohn, T. (2018). Top-down freezing in a fe–fes core and ganymedes present-day magnetic field. *Icarus*, *307*, 172–196.

Safonova, M., Murthy, J., & Shchekinov, Y. A. (2016). Age aspects of habitability. *International Journal of Astrobiology*, *15*(2), 93–105.

Schneider, J., Dedieu, C., Le Sidaner, P., Savalle, R., & Zolotukhin, I. (2011). Defining and cataloging exoplanets: the exoplanet. eu database. *Astronomy & Astrophysics*, *532*, A79.

Schubert, G., & Soderlund, K. M. (2011). Planetary magnetic fields: Observations and models. *Physics of the Earth and Planetary Interiors*, *187*(3-4), 92–108.

Seager, S., Kuchner, M., Hier-Majumder, C., & Militzer, B. (2007). Mass-radius relationships for solid exoplanets. *The Astrophysical Journal*, *669*(2), 1279.

Seagle, C., Heinz, D., Campbell, A., Prakapenka, V., & Wanless, S. (2008). Melting and thermal expansion in the fe–feo system at high pressure. *Earth and Planetary Science Letters*, *265*(3-4), 655–665.

Soubiran, F., & Militzer, B. (2018). Electrical conductivity and magnetic dynamos in magma oceans of super-earths. *Nature communications*, *9*(1), 1–7.

Spergel, D., Gehrels, N., Baltay, C., Bennett, D., Breckinridge, J., Donahue, M., ... others (2015). Wide-field infrarred survey telescope-astrophysics focused telescope assets wfirst-afta 2015 report. *arXiv preprint arXiv:1503.03757*.

Spiegel, D. S., Fortney, J. J., & Sotin, C. (2014). Structure of exoplanets. *Proceedings of the National Academy of Sciences*, *111*(35), 12622–12627.

Stamenković, V., & Breuer, D. (2014). The tectonic mode of rocky planets: Part 1–driving factors, models & parameters. *Icarus*, *234*, 174–193.

Stamenković, V., Noack, L., Breuer, D., & Spohn, T. (2012). The influence of pressure-dependent viscosity on the thermal evolution of super-earths. *The Astrophysical Journal*, *748*(1), 41.

Stanley, S., Zuber, M., & Bloxham, J. (2007). Using reversed magnetic flux spots to determine a planet's inner core size. *Geophysical research letters*, *34*(19).

Stein, C., Schmalzl, J., & Hansen, U. (2004). The effect of rheological parameters on plate behaviour in a self-consistent model of mantle convection. *Physics of the Earth and Planetary Interiors*, *142*(3-4), 225–255.

Stevenson, D. J., Spohn, T., & Schubert, G. (1983). Magnetism and thermal evolution of the terrestrial planets. *Icarus*, *54*(3), 466–489.

Stixrude, L. (2014). Melting in super-earths. *Philosophical Transactions of the Royal Society A: Mathematical, Physical and Engineering Sciences*, *372*(2014), 20130076.

Stixrude, L., de Koker, N., Sun, N., Mookherjee, M., & Karki, B. B. (2009). Thermodynamics of silicate liquids in the deep earth. *Earth and Planetary Science Letters*, *278*(3-4), 226–232.

Strangeway, R., Russell, C., Luhmann, J., Moore, T., Foster, J., Barabash, S., & Nilsson, H. (2010). Does a planetary-scale magnetic field enhance or inhibit ionospheric plasma outflows? *AGUFM*, *2010*, SM33B–1893.

Tackley, P. J., Ammann, M., Brodholt, J. P., Dobson, D. P., & Valencia, D. (2013). Mantle dynamics in super-earths: Post-perovskite rheology and self-regulation of viscosity. *Icarus*, *225*(1), 50–61.

Takahashi, F., & Matsushima, M. (2006). Dipolar and non-dipolar dynamos in a

thin shell geometry with implications for the magnetic field of mercury. *Geophysical research letters*, *33*(10).
Tarduno, J. A., Cottrell, R. D., Watkeys, M. K., Hofmann, A., Doubrovine, P. V., Mamajek, E. E., ... Usui, Y. (2010). Geodynamo, solar wind, and magnetopause 3.4 to 3.45 billion years ago. *science*, *327*(5970), 1238–1240.
Tkalčić, H., Kennett, B. L., & Cormier, V. F. (2009). On the innerouter core density contrast from pkikp/pcp amplitude ratios and uncertainties caused by seismic noise. *Geophysical Journal International*, *179*(1), 425–443.
Valencia, D., O'Connell, R. J., & Sasselov, D. (2006). Internal structure of massive terrestrial planets. *Icarus*, *181*(2), 545–554.
Weiss, L. M., & Marcy, G. W. (2014). The mass-radius relation for 65 exoplanets smaller than 4 earth radii. *The Astrophysical Journal Letters*, *783*(1), L6.
Withers, P., & Vogt, M. F. (2017). Occultations of astrophysical radio sources as probes of planetary environments: A case study of jupiter and possible applications to exoplanets. *arXiv preprint arXiv:1702.07075*.
Wohlers, A., & Wood, B. J. (2017). Uranium, thorium and ree partitioning into sulfide liquids: Implications for reduced s-rich bodies. *Geochimica et Cosmochimica Acta*, *205*, 226–244.
Wood, B. J., Walter, M. J., & Wade, J. (2006). Accretion of the earth and segregation of its core. *Nature*, *441*(7095), 825–833.
Zhang, T., Baumjohann, W., Russell, C., Luhmann, J., & Xiao, S. (2016). Weak, quiet magnetic fields seen in the venus atmosphere. *Scientific reports*, *6*, 23537.

Supporting Information for "Structure and thermal evolution of exoplanetary cores"

Irene Bonati[1], Marine Lasbleis[1,2], and Lena Noack[3]

[1]Earth-Life Science Institute, Tokyo Institute of Technology, Tokyo 152-8550, Japan

[2]Laboratoire de Planétologie et Géodynamique, LPG, UMR 6112, CNRS, Université de Nantes, Université d'Angers, France

[3]Department for Earth Sciences, Freie Universität Berlin, Malteserstr. 74-100, D-12249 Berlin, Germany

Contents of this file

Figure S1.

Inner core radius fractions after 5 Gyr of evolution

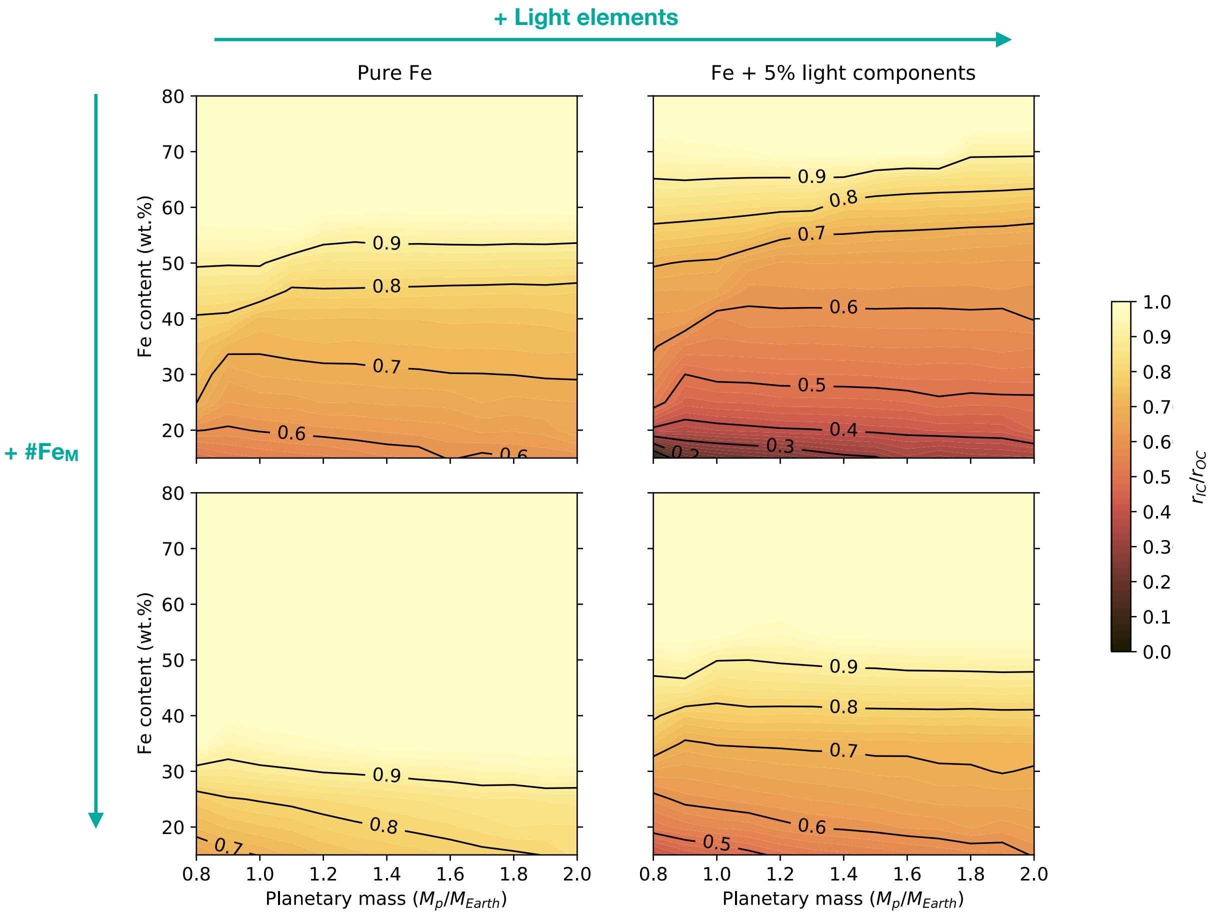

Radial fraction of the inner core ($r_{\mathrm{IC}}/r_{\mathrm{OC}}$) after 5 Gyr of evolution as a function of planetary mass, bulk iron content, mantle iron number (upper row: $\#Fe_{\mathrm{M}} = 0$, lower row: $\#Fe_{\mathrm{M}} = 0.1$), and core composition (left column: pure iron, right column: iron and 5% light elements).

Figure S2.

L_ρ (left) and A_ρ (right) for a range of planetary masses and iron contents. Values for Earth are $L_\rho = 7683$ km and $A_\rho = 0.484$ (Labrosse, 2015).

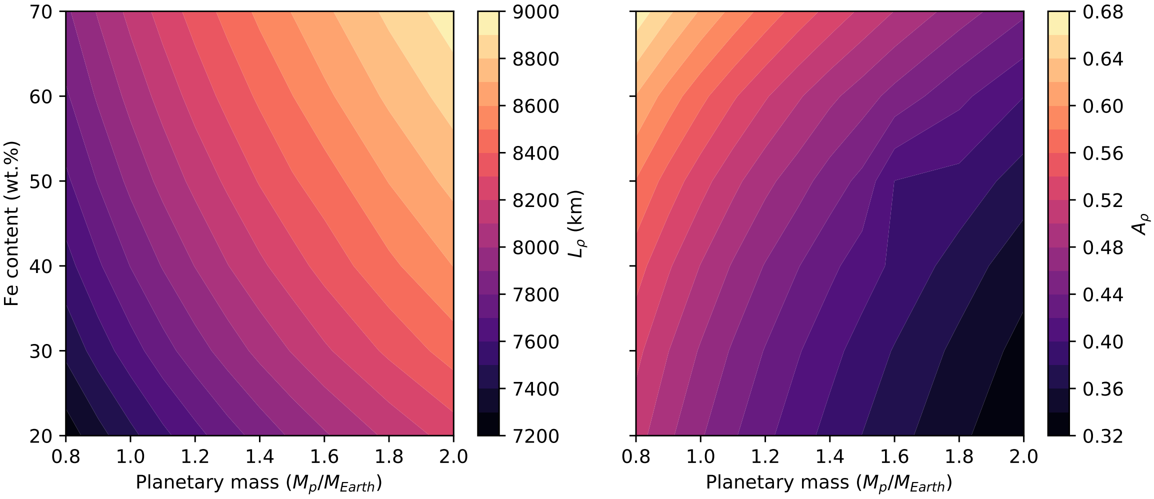

Figure S3.

Inner core radius fractions at the beginning (end of accretion) and at the end (5 Gyr later) for planets with a mantle iron number $\#Fe_{\mathrm{M}} = 0.2$. The core is made of pure iron (left panel) and iron with 5 % of light elements (right panel)

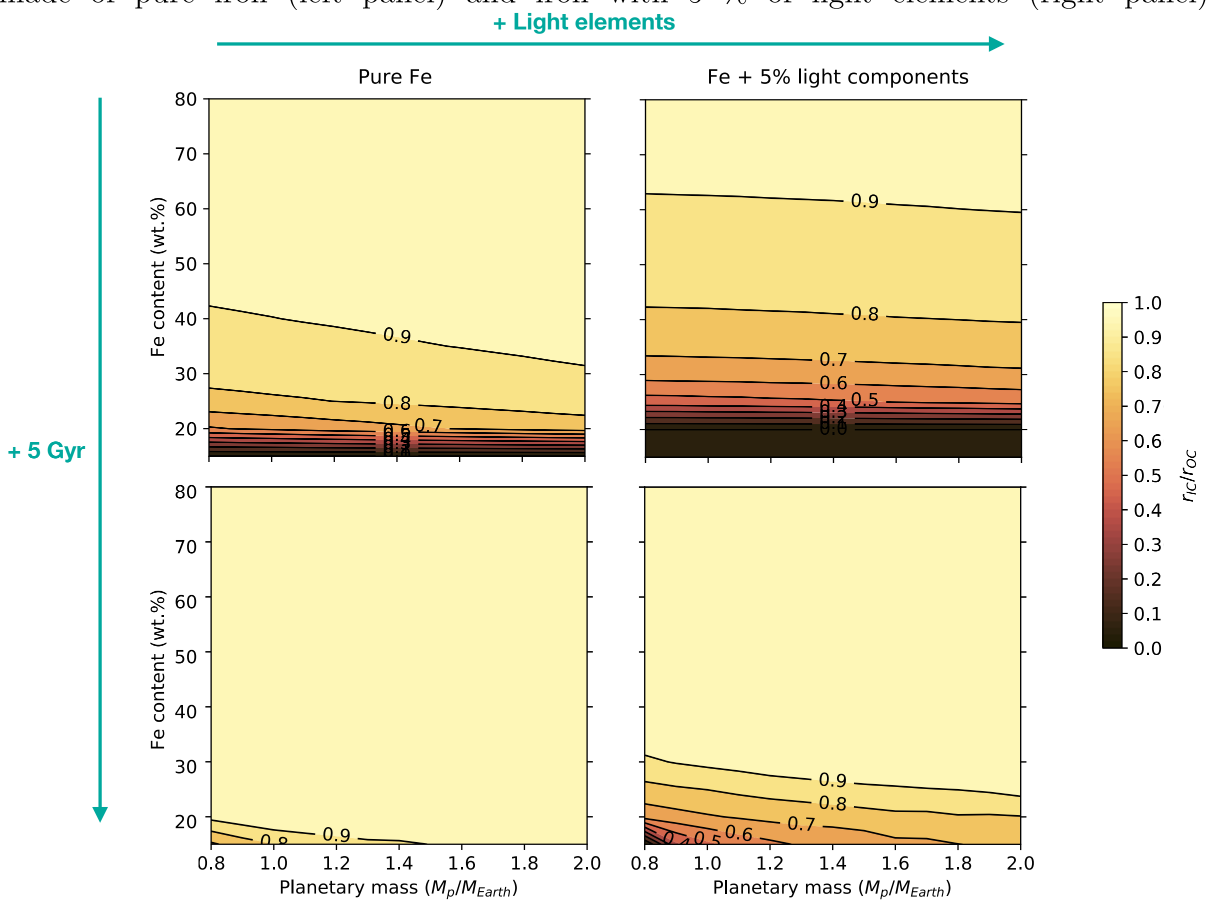

References

Labrosse, S. (2015). Thermal evolution of the core with a high thermal conductivity. *Physics of the Earth and Planetary Interiors*, *247*, 36–55.